A&A 672, A115 (2023)
https://doi.org/10.1051/0004-6361/202245453

Astronomy & Astrophysics

Space weathering effects and potential spectral alteration on Phobos and the Moon: Clues from the Fe content of olivine

Jingyan Xu (徐静妍)[1,2], Bing Mo (莫冰)[2,3,4,5], Yanxue Wu (吴焱学)[6], Yu-Yan Sara Zhao (赵宇鹓)[2,5,7], Honglei Lin (林红磊)[8], Binlong Ye (叶斌龙)[9], Joseph Michalski[9], Yang Li (李阳)[2,5], Kairui Tai (郃凯瑞)[7], Chen Li(李琛)[2], Zhuang Guo (郭壮)[2], Chao Qi (綦超)[8,4], Shen Liu (刘燊)[1], Xiongyao Li (李雄耀)[2,5], and Jianzhong Liu (刘建忠)[2,5]

[1] State Key Laboratory of Continental Dynamics and Department of Geology, Northwest University, Xi'an 710069, PR China
e-mail: liushen@nwu.edu.cn
[2] Center for Lunar and Planetary Sciences, Institute of Geochemistry Chinese Academy of Sciences, Guiyang 550081, PR China
e-mail: zhaoyuyan@mail.gyig.ac.cn
[3] State Key Laboratory of Ore Deposit Geochemistry, Institute of Geochemistry Chinese Academy of Sciences, Guiyang 550081, PR China
[4] College of Earth and Planetary Sciences, University of Chinese Academy of Sciences, Beijing 100049, PR China
[5] CAS Center for Excellence in Comparative Planetology, Hefei 230026, PR China
[6] Analysis and Test Center, Guangdong University of Technology, Guangzhou 510006, PR China
[7] Research Center for Planetary Science, College of Earth Science, Chengdu University of Technology, Chengdu 610059, PR China
[8] Key Laboratory of Earth and Planetary Physics, Institute of Geology and Geophysics, Chinese Academy of Sciences, Beijing 100029, PR China
[9] Department of Earth Sciences, University of Hong Kong, Hong Kong 999077, PR China

Received 13 November 2022 / Accepted 31 January 2023

ABSTRACT

Context. Olivine responds to space weathering in the fastest and most profound way, which results in significant space weathering spectral alteration effects (SWSAEs) on airless silicate bodies. Although Mg-rich olivine (Fa_{10}) has been subjected to extensive studies, SWSAEs of Fe-rich (Fa# > 20) or Fa-dominant (Fa# ⩾ 50) olivine are still poorly understood.
Aims. We aim to systematically characterize the space weathering effects and the associated spectral alterations of Fe-rich olivine on the surface of Phobos and the Moon.
Methods. We conducted nanosecond pulsed laser irradiation experiments on a set of synthetic Fe-rich olivine (Fa_{29}, Fa_{50}, Fa_{71}, and Fa_{100}) with energy levels simulated for Phobos and the Moon and analyzed the irradiated olivine for microscopic characteristics and near-infrared (NIR) and Raman spectroscopy.
Results. Micron-level thick alteration layers are found in Fa_{100} compared to those hundreds of nanometers thick in Fa_{29}, Fa_{50}, and Fa_{71}. With increasing irradiation energy levels and Fa# values, nanophase iron (np-Fe^0) particles increase in size but decrease in quantity. The np-Fe^0 formed via in situ decomposition are ubiquitously present, while those formed via vapor deposition are primarily found in Fa_{29} but rarely in Fa# ⩾ 50. The size fraction of intermediate (10–40 nm) and large (40–60 nm) np-Fe^0 proportionally increases with Fa# values. The NIR spectra of weathered olivine show darkening over reddening in most cases, but Fa_{100} under the most irradiated condition shows brightening-reddening spectral effects. The Raman spectra of weathered olivine show a reduction in intensity without peak shifts.
Conclusions. The Fa# values of olivine are a more critical factor in controlling the SWSAEs on Phobos than those on the Moon. If Phobos and Deimos contain substantial Fe-rich or Fa-dominant olivine, similar to Mars, thick alteration rims and large np-Fe^0 formed via space weathering may cause darkening-reddening and potentially brightening-reddening spectral effects on the Martian moons.

Key words. planets and satellites: surfaces – methods: analytical – meteorites, meteors, meteoroids

1. Introduction

The surface of airless bodies is subjected to long-term space weathering. While various processes may simultaneously contribute to space weathering, for inner Solar System bodies, the dominant processes are cosmic irradiation, solar wind, and micrometeoroid bombardment (Hapke 2001; Pieters & Noble 2016). For a specific celestial body, the effects of space weathering are determined by a combination of factors, including its position in the Solar System (e.g., impact velocity and flux, radiation environment, and temperature), compositions, physical properties, and exposure history of the surface materials (Pieters & Noble 2016; Weber et al. 2020).

Previous studies of the Moon and S-type asteroids suggested that olivine responds to space weathering in the fastest and most profound way due to the formation of nanophase iron (np-Fe^0) particles (see e.g., Kohout et al. 2014; Sasaki et al. 2001). The formation of np-Fe^0 particles along with other nanophase opaque particles, amorphization, and the formation of vesicles are the primary cause of alteration of optical properties of the airless bodies, namely, space weathering spectral alteration effects (SWSAEs), including reduced spectral reflectance (darkening), increased spectral slope (reddening), and reduced particular absorption bands in the ultraviolet to visible and near-infrared (NIR) reflectance spectra (see e.g., Chrbolková et al. 2022; Hapke 2001; Pieters & Noble 2016). In contrast, pyroxene,

another primary rock-forming mineral on a silicate celestial body, is more resistant to the formation of np-Fe^0, and therefore its reflectance spectra are less affected than those of olivine during space weathering processes (Pieters & Noble 2016; Sasaki et al. 2002; Yamada et al. 1999).

Since np-Fe^0 particles were discovered in the lunar samples returned by the Apollo mission, substantial efforts have been made to investigate space weathering effects on olivine, including the analysis of meteorites and returned samples, laboratory simulation experiments, spectral analyses, and modeling. These studies included a comparison of space weathering effects on olivine induced by solar wind implantation versus micrometeoroid and dust impacts (see e.g., Chrbolkova et al. 2021; Yamada et al. 1999); formation mechanisms of np-Fe^0 in olivine (see e.g., Keller & McKay 1997; Noble et al. 2007; Vandemoortele et al. 2007; Wang et al. 2012); atomic-level mechanisms for the favorable formation of np-Fe^0 in olivine rather than in pyroxene (Quadery et al. 2015; Shilobreeva et al. 2014); the influence of sizes and amounts of np-Fe^0 particles on reflectance spectra of olivine (see e.g., Kohout et al. 2014; Markley & Kletetschka 2016); and the infrared spectral inversion model for detecting and quantifying olivine (see e.g., Cloutis et al. 2015; Han et al. 2020; Pinet et al. 2022; Yang et al. 2017). However, previous studies almost exclusively focused on Mg-rich olivine (e.g., San Carlos olivine) and rarely involved Fe-rich olivine. Although a spectral library of the synthetic forsterite-fayalite solid solution set is available (Dyar et al. 2009; Pinet et al. 2022), it generally lacks data of the same set after being space-weathered. How Fe-rich olivine (Fa# > 20; Fa# represents Fe mol%), or even fayalite-dominant olivine (Fa # ⩾ 50), responds to a specific space weathering process (e.g., micrometeoroid impacts, solar wind sputtering) in terms of the microscopic characteristics and optical properties is poorly understood.

Newly returned Chang'E-5 (CE-5) lunar samples (Li et al. 2021) and the planned exploration mission to the Martian moons, such as the Martian Moons exploration mission by the Japan Aerospace Exploration Agency (Kuramoto et al. 2022) make the need for this perspective more urgent. The CE-5 lunar regolith is young and composed of fayalitic olivine compared to the older and Mg-rich Apollo sample (Li et al. 2021). Different dominant space weathering processes and new np-Fe^0 formation mechanisms (i.e., thermal decomposition, Fe disproportionation) have been identified in olivine through these less mature regolith samples (Guo et al. 2022; Li et al. 2022; Mo et al. 2022).

Martian moons (Phobos and Deimos) generally lack apparent diagnostic absorption features and are considered the most enigmatic airless bodies (Pieters & Noble 2016). The originating materials of Deimos and the dominant red unit of Phobos are similar (Fraeman et al. 2012). However, whether Phobos and Deimos originated by capture (i.e., D-type asteroid) or formation in situ due to impact events around Mars is difficult to ascertain (Usui et al. 2020). More recent numerical simulations have proposed that Phobos and Deimos may have formed in situ from debris related to giant impacts (Bagheri et al. 2021; Canup & Salmon 2018; Citron et al. 2015; Hyodo et al. 2017). If that is the case, the original building blocks of Phobos and Deimos may involve Fe-rich olivine, as it is globally present in the Martian crust (Koeppen & Hamilton 2008). Subsequent space weathering of Fe-rich olivine might be the key attribute to the substantial dark signatures and the lack of mineralogical absorption signatures of these moons compared to other asteroids.

This study is one of a series of works systematically investigating space weathering effects on Fe-rich olivine. In this study, we conducted nanosecond pulsed laser irradiation experiments using a set of synthetic Fe-rich olivine (Fa_{29}, Fa_{50}, Fa_{71}, and Fa_{100}). The pulsed laser irradiation experiments best simulate the thermal effects induced by micrometeoroid impacts (Hamann et al. 2016; Weber et al. 2020). Three energy levels (5 mJ × 1, 5 mJ × 5, and 5 mJ × 15) were examined to simulate the levels for Phobos, and two energy levels (15 mJ × 5 and 15 mJ × 10) were examined to simulate the levels for the Moon. This work provides essential microscopic characteristics, NIR and Raman spectral data, and quantitative inputs for spectral simulation of the space-weathered Fe-rich olivine.

2. Materials and methods

2.1. Synthetic Fe-rich olivine and characterization

The fayalite (Fa_{100}) end-member was synthesized in the furnace using powders of Fe_2O_3 and SiO_2 in a molar ratio of 1:1.002 at temperatures close to the melting point of fayalite under a controlled oxygen buffer (using a gas mixture of CO_2 and CO). The samples of Fa_{71}, Fa_{50}, and Fa_{29} were then fabricated by mixing the synthetic fayalite with commercial forsterite. The mixtures were ground to a particle size of <25 µm and reacted at ~85% of the solidus temperature in a one-atmosphere furnace for 20 h under a controlled oxygen buffer (Qi et al. 2021; Zhao et al. 2009).

The synthetic Fe-rich olivine samples were pure and crystalline, as confirmed by powder X-ray diffraction (Fig. A.1). The X-ray diffraction patterns were collected through a Panalytical Empyrean diffractometer at the State Key Laboratory of Ore Deposit Geochemistry, Institute of Geochemistry, Chinese Academy of Sciences. All patterns were collected using Cu-Kα radiation (λ = 1.5419 Å) at 45 kV and 40 mA in the range of 10°–60° 2θ, a step size of 0.0263°, and a counting time of 36.465 s per step. The chemical compositions of Fe-rich olivine samples were determined by an inductively coupled plasma emission spectrometer (ICP735-ES) after acid digestion. The synthetic olivine samples comprised FeO, MgO, and SiO_2, with minor Al_2O_3, CaO, MnO, and Ni contents (Table A.1).

Due to the excess of initial SiO_2 in synthesizing the Fa_{100}, slight SiO_2 residuals were expected to be present in the synthetic olivine (Fig. A.2). As shown in previous studies, the SiO_2 residuals do not influence the physical, mechanical, or spectral characteristics of the synthetic olivine (see e.g., Qi et al. 2021; Zhao et al. 2009). However, caution was taken when interpreting the SiO_2-relevant results on the microscopic scale, such as the TEM results.

2.2. Settings of laser irradiation simulation experiments

The synthetic olivine samples were ground and sieved into powder with a grain size <75 µm. They were dried at 80 °C for 8 h and then compressed into pellets (13 mm diameter and 2 mm thickness) to serve as the laser irradiation targets.

The choice of laser irradiation energies was based on the micrometeoroid flux and impact velocities at the Phobos and Moon locations and the size of the laser spots (Table 1). The equivalent space weathering timescale by laser irradiation in this study can be roughly estimated by the ratio of the calculated energy density (i.e., the total deposition energy by laser per square meter on the samples) to the deposited energy per square meter per year on the airless bodies (Zhang et al. 2022). The micrometeoroid impact flux was estimated to be the same for Phobos and the Moon at 10^{-4} m^{-2} s^{-1} (Grün et al. 1991). For Phobos, the micrometeoroid impact velocity ranged from 8.62

Table 1. Parameter settings of laser irradiation experiments.

Targets	Solar distance	Impact flux (F)	Impact velocity (v)	Experimental condition abbr.	Laser single-shot energy	Shot times	Laser total energy (TE)	Equivalent years of space weathering (C)
Phobos	1.5 Au	10^{-4} m^{-2} s^{-1}	8.62–12 km s^{-1}	P5 mJ	5 mJ	1	5 mJ	0.1 Ga
				P25 mJ		5	25 mJ	1 Ga
				P75 mJ		15	75 mJ	2 Ga
The Moon	1.0 Au		15 km s^{-1}	M75 mJ	15 mJ	5	75 mJ	1 Ga
				M150 mJ		10	150 mJ	2 Ga

Notes. The equivalent space weathering years by our simulation experiments can be roughly estimated by assuming that all kinetic energy from micrometeoroid bombardments on asteroids would convert into heat and that the micrometeoroid flux does not change over time (Zhang et al. 2022). The equivalent years of space weathering was calculated using the formula $C = B / A$, where B denotes the energy density (i.e., total deposited energy by laser per square meter in our experiments) and A denotes the deposited energy per square meter per year on airless bodies. The formula to calculate B is $B = TE/\pi\ r^2$, where TE represents the laser total energy in our experiment (unit in J) and r represents the radius of each laser spot (i.e., 2.5×10^{-4} m) in our experiments. The formula to calculate A is $A = 1/2\ mv^2\ FT$, where m represents the mass of each dust particle (i.e., 10^{-15} kg), v represents impact velocity (i.e., 15 km s^{-1} for the Moon and 8.62–12 km s^{-1} for Phobos), F represent impact flux (i.e., 10^{-4} m^{-2} s^{-1}), and T represents impact time (i.e., $365 \times 24 \times 3600$ s).

to 12 km s^{-1} (Ballouz et al. 2019; Divine 1993; Miyamoto et al. 2021), so the total energy for the Phobos surface ranged from 2.23 to 178 mJ. For the lunar surface, the micrometeoroid impact velocity was estimated to be 15 km s^{-1} (Divine 1993); thus, the total energy ranged from 69.6 to 139 mJ. Due to the different micrometeoroid impact velocities on the surfaces of Phobos and the Moon and the corresponding kinetic energies, we assigned one level of single-shot energy to simulate Phobos (5 mJ) and another to simulate the Moon (15 mJ). Considering the size of the laser spots (0.5 mm in diameter), we ultimately set three energy levels for Phobos: 5 mJ × 1(P5mJ), 5 mJ × 5 (P25mJ), and 5 mJ × 15 (P75mJ), and we set two energy levels for the Moon: 15 mJ × 5 (M75mJ) and 15 mJ × 10 (M150mJ). The conditions P75mJ (5 mJ × 15) and M75mJ (15 mJ × 5) were set to compare the effects caused by the single-shot energy level when the total energy level remained the same. The equivalent space weathering timescale by laser irradiation in this study (listed in Table 1) can be roughly estimated by the ratio of the calculated energy density (i.e., the total deposition energy by laser per square meter on the samples) to the deposited energy per square meter per year on the airless bodies (Zhang et al. 2022).

The pulsed laser irradiation simulation experiments were conducted using the ultrahigh vacuum surface analysis system at the Institute of Geochemistry, Chinese Academy of Sciences. A Continuum Surelite I-10 laser was used with a wavelength of 532 nm, and the pulse duration was 6–7 ns, which is comparable to the timescale of micrometeoroid impact (Yamada et al. 1999). The olivine pellets were individually placed in a custom-made sample tank, fixed, and placed in the vacuum chamber. The vacuum condition during the irradiation experiment was 1.8×10^{-4} to 2.4×10^{-6} Pa. The laser light path was horizontal, and the target pellets were placed perpendicular to the laser light path. Each set of laser irradiations produced a clear bombardment pit of 0.5 mm in diameter. To enable subsequent sample analysis, the bombardment pits were arranged as a matrix on the pellet surface. The target pellets were stored in the vacuum desiccator before and after the experiments.

2.3. Sample analysis

Near-infrared reflectance spectra were collected in the Planetary Spectroscopy and Mineralogy Laboratory at the University of Hong Kong. A Nicolet Continuum Infrared microscope attached to the Thermal Nicolet iS50 spectrometer with an Indium Gallium Arsenide (InGaAs) detector was used to collect NIR reflectance spectra in situ on the pellet samples. Reflectance spectra were collected in a range from 1 μm to 2.5 μm with a spectral resolution of 8 cm^{-1} using a gold reflectance standard. To obtain high-quality spectra of each sample, a 150 μm aperture size and 128 scan integrations over 4 min were used.

The Raman spectra were collected before and after laser irradiation using a Renishaw inVia laser Raman spectrometer with a 532 nm laser and scanned from 100 cm^{-1} to 4000 cm^{-1}. The spectral analysis rate was 1.3 cm^{-1}, and the spectral repeatability was less than ±0.15 cm^{-1}. For each target pellet, ten pits were analyzed under a 50× microscope with a laser power of 1 mW. The integration time per spectrum was 30 s.

The surface of the laser-irradiated bombardment pits on each target pellet was sampled by a focused ion beam (FIB) for detailed characterization. The FIB sampling was conducted using FEI Scios Dual-Beam scanning electron microscopy (SEM) at the Institute of Geochemistry, Chinese Academy of Sciences. Before FIB sampling, the sample surface was plated with a platinum coating to prevent damage caused by the Ga^+ ion. For each pellet, the FIB sampling positions were consistent and confined at the center bottom of the bombardment pits to enable comparison across the different pellets. The FIB-sampled thin foils were characterized using a Talos F200S transmission electron microscope (TEM) at 200 kV at the Analysis and Testing Center of Guangdong University of Technology. The TEM analysis included TEM bright field imaging, dark-field imaging, high-angle annular dark-field scanning transmission electron microscopy (HAADF-STEM) imaging, and energy dispersive spectrometry (EDS) X-ray energy spectroscopy (detection limit 0.1–0.5 wt%).

Four samples (Fa_{100}-P75mJ, Fa_{100}-M150mJ, Fa_{71}-P75mJ, and F_{71}-M150mJ) were analyzed by electron microscope-electron energy loss spectroscopy (EELS) for the distribution of Fe valence. These samples represent Fa_{100} and Fa_{71}, which experienced the highest total irradiation energies on the surface of Phobos and the Moon, respectively. The TEM-EELS analysis was conducted using a Gatan GIF Quantum ER system Model 965 parallel EELS spectrometer attached to a Hitachi HF5000 TEM at the Shanghai Institute of Ceramics, Chinese Academy of Sciences. The accelerating voltage was 200 kV, and the energy resolution at the zero-loss peak was 0.5–0.7 eV. The full width at half maximum (FWHM) spectra were acquired in DualEELS mode using a probe current of 100 pA. The acquisition time

for each point analysis was 4.5 s. Reference standards of Fe^{2+} and Fe^{3+} for the TEM-EELS analysis were prepared using the synthetic fayalite and hematite extract, respectively, from an ordinary chondrite meteorite (GRV051874).

3. Results and discussion

3.1. Characteristics of laser irradiation pits

Before laser irradiation, the olivine powders showed gradual variations from white (Fa_{29}) to dark green (Fa_{100}) with increasing Fe content (Fig. A.3). After irradiation, the laser-irradiated pits were visually darkened, and the color deepened with increasing irradiation energy (Fig. 1). The SEM images showed the melting and cementing of initial olivine particles (Fig. A.4) and produced a glassy surface from which the FIB foils were taken (Fig. A.5).

3.2. Structures of laser alteration layers on the olivine rim

The laser irradiation produced multilayer structures at the rims of the olivine grains, and the produced structures varied in response to different olivine types and irradiation energy levels. Pure fayalite (Fa_{100}) produced two altered structures depending on the irradiation energy. Under P5mJ and P25mJ conditions, the olivine surface produced a three-layered structure with a thin vapor deposition layer (top), an amorphous layer (middle), and the olivine host (basal; Figs. 2a,c). Under P75mJ to M150mJ conditions, the irradiated rim also consisted of three layers. The vapor deposition layer on top was absent, and a subsolidus layer appeared beneath the amorphous layer (Fig. 2d). The crystallographic orientation of the subsolidus layer was identical to that of the olivine host (Figs. 2h and A.6a), suggesting that it was not formed by recrystallization of the amorphous melts during cooling but was instead a remnant of the precursor olivine host (Fazio et al. 2018; Weber et al. 2020). The np-Fe^0 particles were identified throughout the laser-altered layers, having a lattice spacing of 0.203 nm, consistent with the lattice plane (110) of α-Fe (Fig. 2b).

Both Fa_{71} and Fa_{50} consistently produced three-layered structures (amorphous plus subsolidus plus basal olivine host) under all irradiation conditions (Figs. 2e–j), similar to those observed in Fa_{100} under high-energy conditions (P75mJ to M150mJ). Under irradiation conditions from P5mJ to M75mJ, Fa_{29} produced a four-layered structure. In this structure, the vapor deposition layer was consistently present on top of the amorphous plus subsolidus plus basal olivine host structure (Fig. 2k). However, under the highest energy condition (M150mJ), a vapor deposition layer with np-Fe^0 particles included was not observed (Fig. 2l).

In addition, irradiation induced splash materials, vesicles, and amorphous silica were also observed in the laser-irradiated olivine. The splash materials were deposited on top of the amorphous layer containing no np-Fe^0 particles (Fig. A.6). Two types of splash materials were identified. One shared the same composition as the underlying amorphous layer (Figs. A.6a–d), and the other was relatively Si-poor (Figs. A.6e–h). In addition, a large number of vesicles with various sizes were identified as being widely distributed in the amorphous layer and close to the np-Fe^0 particles (Fig. 3). Amorphous silica was also observed (Fig. 3a), but many residual SiO_2 originated from synthesizing the Fe-rich olivine samples (Fig. A.1).

Similar to the vapor deposition layer observed in magnesian olivine in lunar or analog samples (see e.g., Sasaki et al. 2001), Fa_{29} consistently produced a vapor deposition layer. The vapor layer was absent under the highest irradiation energy condition (M150mJ), which is consistent with a previous report that used Fa_{09} and even higher energy (i.e., 15 mJ × 20; 300 mJ) (Weber et al. 2020). In contrast, most Fa-dominant olivine samples (Fa_{50}, Fa_{71}, and Fa_{100}) produced mainly amorphous and subsolidus layers without a vapor deposition layer. An exception to this occurred in Fa_{100} under low-energy conditions (P5mJ and P25mJ), where a very thin veneer (a few nanometers thick) was present.

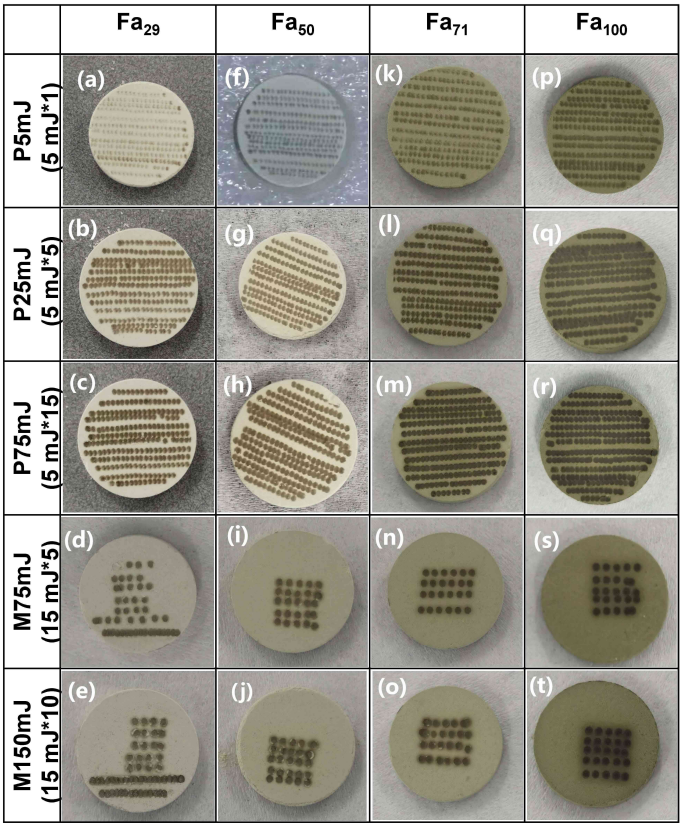

Fig. 1. Target pellets of four types of olivine after laser irradiations. Each pellet is 13 mm in diameter and 2 mm in thickness. The four olivine types are Fa_{29} (a–e), Fa_{50} (f–j), Fa_{71} (k–o), and Fa_{100} (p–t). The five irradiation energies used were P5mJ (first row), P25mJ (second row), P75mJ (third row), M75mJ (fourth row), and M150mJ (fifth row). The dark spots lined up in a matrix on each pellet are the laser irradiation spots (0.5 mm in diameter), and the light-tone area is the initial state of the olivine. The initial color of the pellets became darker with increasing Fa# values. After irradiation, the color of the irradiation spots became substantially darker. In addition, the color tones became darker as the total energies increased.

3.3. Thickness of the laser alteration layer

The laser alteration layer refers to the sum of altered layers above the basal olivine host, including the vapor depositional, amorphous, and subsolidus layers. For each type of olivine, the thickness of the laser alteration layer positively correlated with the irradiation energy (Fig. 4). Upon increasing from P5mJ to M150mJ, the laser alteration layer of Fa_{29} to Fa_{100} increased from ~200–1700 nm. The two conditions P75mJ (5mJ × 15) and M75mJ (15mJ × 5) further suggested that higher single-shot energy would consistently produce a thicker laser alteration layer across all the olivine (Fig. 4).

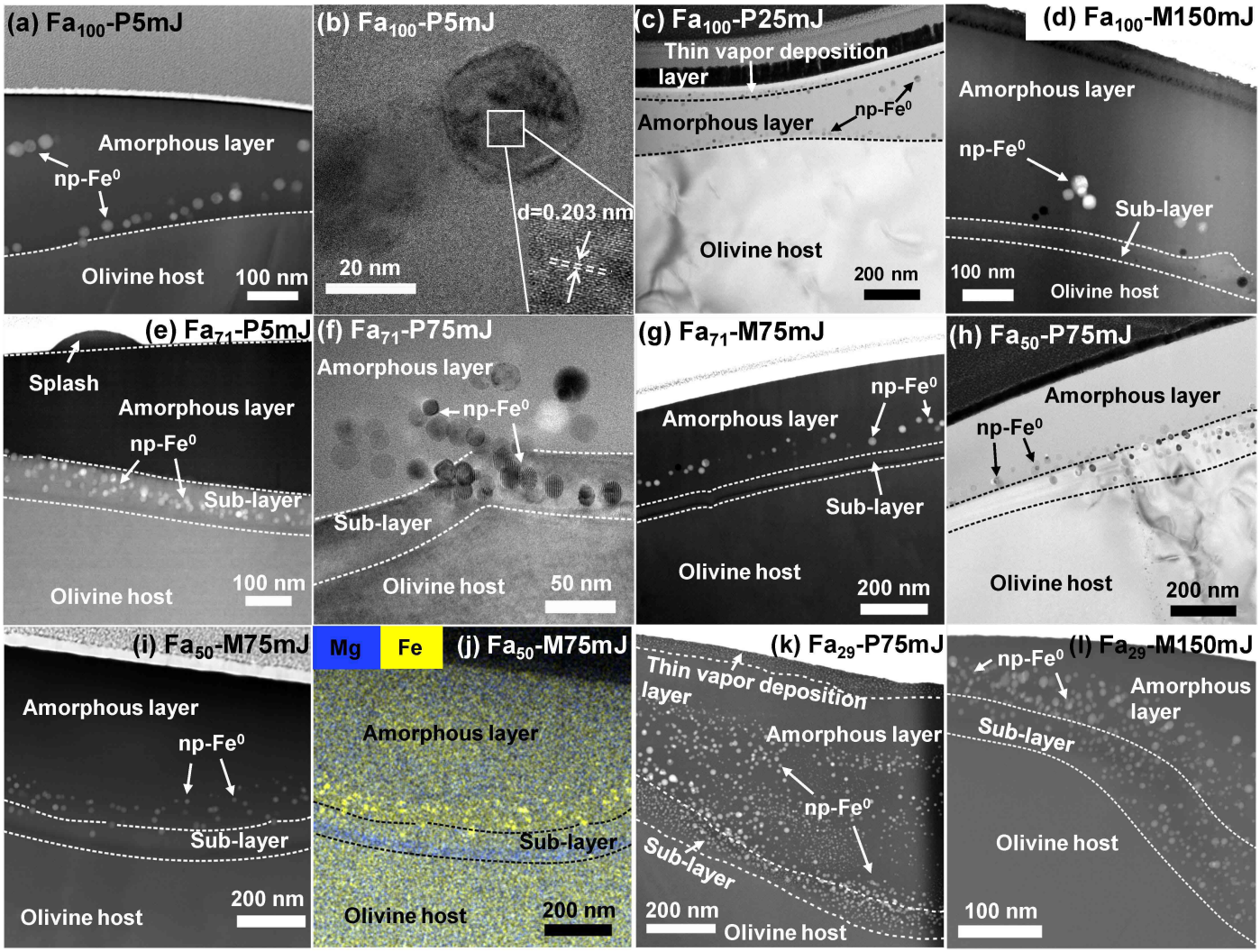

Fig. 2. TEM images of different layered structures. Image (a) Fa_{100}-P5mJ with a two-layer structure: amorphous layer plus olivine host. Image (b) High-resolution TEM image of np-Fe^0 distributed in the middle and bottom of the amorphous layer in image (a). The interplanar spacing is d = 0.203 nm, which is consistent with a crystal lattice plane (110) of α-Fe. Image (c) Fa_{100}-P25mJ with a three-layer structure: vapor deposition layer plus amorphous layer plus olivine host. Image (d) Fa_{100}-M150mJ with a three-layer structure: amorphous layer plus subsolidus layer plus olivine host that differs from that of image (c). Image (e) Fa_{71}-P5mJ, (f) Fa_{71}-P75mJ, (g) Fa_{71}-M75mJ, (h) Fa_{50}-P75mJ, and (i) Fa_{50}-M75mJ in which the three-layer structure represents most of the samples: amorphous layer plus subsolidus layer plus olivine host. Image (j) EDS mapping of (i) showing the elemental distribution of Mg and Fe. Image (k) represents the characteristics of Fa_{29} in the energy range from P5mJ to M75mJ and with a four-layer structure: vapor deposition layer plus amorphous layer plus subsolidus layer plus olivine host. Image (l) shows Fa_{29}-M150mJ with a three-layer structure: amorphous layer plus subsolidus layer plus olivine host. This figure shows the variation in the layer structure produced by olivine with different iron contents at different energy levels.

The relative thickness of laser alteration layers in the different types of olivine changed with irradiation energy levels. Positive correlations between the layer thickness and Fa# values were found only at the P5mJ condition. Under the P25mJ condition, Fa_{29}, Fa_{50}, and Fa_{71} produced alteration layers similar in thickness, and the overall pattern was in the order of $Fa_{100} \gg Fa_{29} \approx Fa_{50} \approx Fa_{71}$. At higher energy levels (P75mJ to M150mJ), the relative thickness patterns were in the order of $Fa_{100} \gg Fa_{29} > Fa_{71} > Fa_{50}$. Of all the types of Fe-rich olivine, Fa_{100} formed alteration layers substantially thicker than those of the Fo–Fa solid-solution samples, except under the lowest energy condition (Fig. 4). For most energy levels in our experiments, alteration layers of Fa_{100} reached the micron level. In contrast, the other Fo-Fa solid-solution samples produced alteration layers only hundreds of nanometers thick.

Notably, the thickness of the alteration layers in Fa_{29}, Fa_{50}, and Fa_{71} did not correlate to their Fa# values, as presumed. In particular, Fa_{50} constantly produced a thinner alteration layer than Fo-dominant Fa_{29} and Fa-dominant Fa_{71}. This discrepancy might be attributable to the degree of nonideal solid-solution present in Fa_{50}, as Fa_{29} and Fa_{71} demonstrate fewer nonideal characteristics when either forsterite or fayalite is predominant in their structures. Although we did not identify an outstanding difference in the initial Fa_{50} compared to previous studies of Fo–Fa solid solutions (Kuebler et al. 2006), we infer that the case of nonideal solid solutions might be most pronounced in Fa_{50}, and such a difference can be amplified during nonequilibrium processes, such as laser-induced alteration. Potentially similar nonideal conditions were observed in a grossular-pyrope solid solution in which the most significant deviations appeared

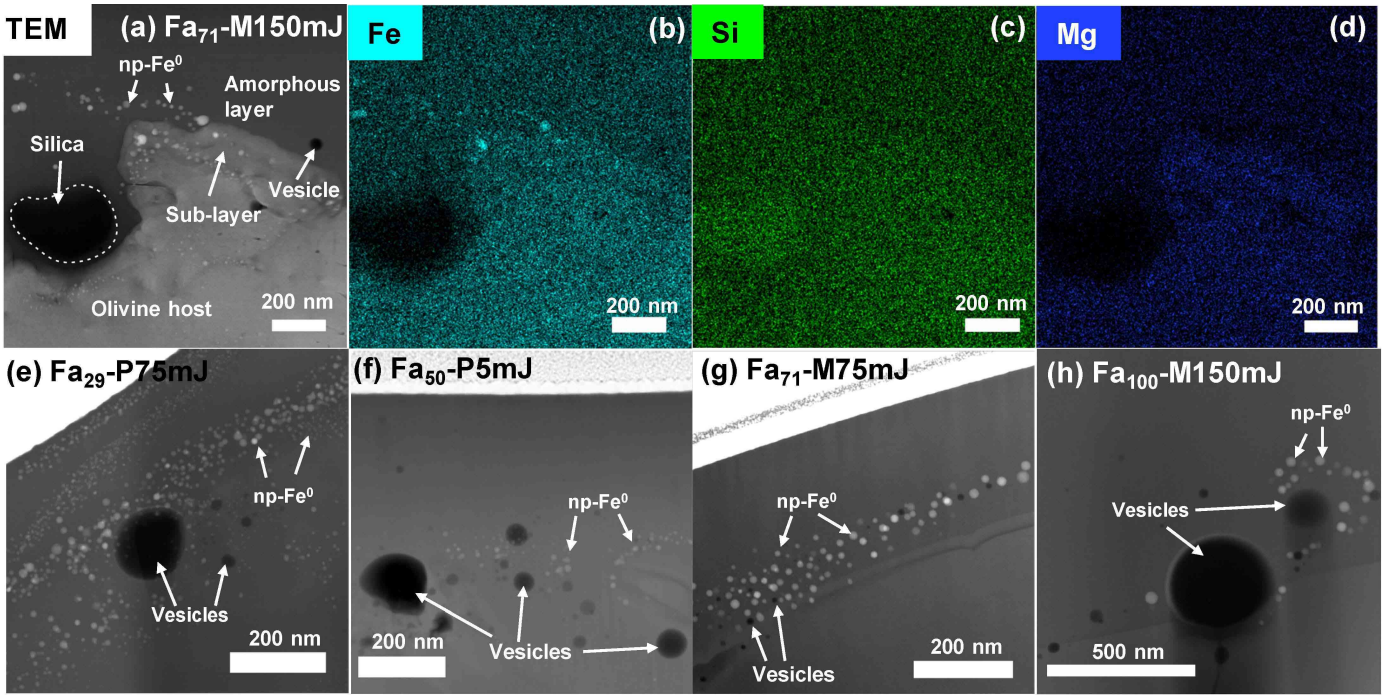

Fig. 3. Vesicles and amorphous silica by laser irradiated in olivine. Image (a) TEM image of Fa_{71}-M150mJ containing np-Fe^0, amorphous silica, and vesicle. Image (b) Fe, (c) Si, and (d) Mg as EDS mapping images in image (a). Image (e) Fa_{29}-P75mJ, (f) Fa_{50}-P5mJ, (g) Fa_{71}-M150mJ, and (h) Fa_{100}-M150mJ showing features containing np-Fe^0 and vesicles. Vesicles support the in situ decomposition reaction of olivine. The EDS mapping shows that the area framed by the white dashed curves in Fig. 3a is amorphous silica, which may be residual SiO_2 that originates from synthesizing the Fe-rich olivine samples.

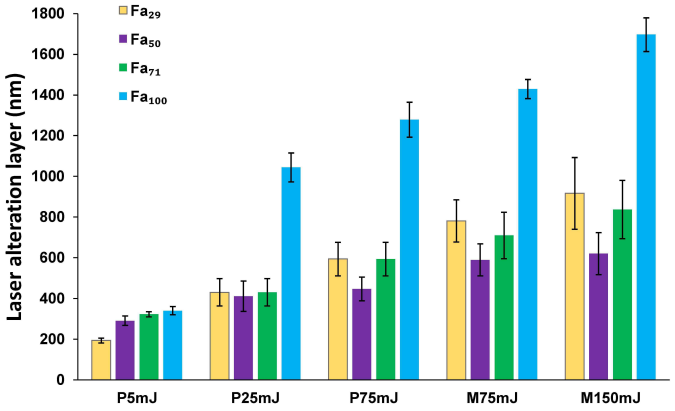

Fig. 4. Comparison of the thickness of the laser alteration layer formed in different types of olivine and irradiation energies. Four types of olivine, Fa_{29} (yellow), Fa_{50} (in purple), and Fa_{71} (in green), Fa_{100} (in blue), and five total energy levels (P5mJ, P25mJ, P75mJ, M75mJ, and M150mJ) were compared. The bars represented median values of the laser alteration layer thicknesses. The thicknesses of the laser alteration layer of Fa_{29}, Fa_{50}, and Fa_{71} are not significantly different at the same energy, and the thickness of the laser alteration layer produced by Fa_{100} is significantly thicker than the other groups with increasing energy. At different energies, the thickness of the laser alteration layer was positively correlated with the Fe content.

when end-members were mixed at a ratio of one to one (Du et al. 2017).

3.4. Characteristics of np-Fe^0 particles

The np-Fe^0 particles showed distinct characteristics in different layers. In the vapor deposition layer, the np-Fe^0 particles were evenly distributed and concentrated in the upper part of the layer if the layer thickness was greater than the size of the np-Fe^0 particles (Fig. A.7). In the amorphous and subsolidus layers, the np-Fe^0 particles were uniformly distributed in the subsolidus layer and tended to merge and migrate into the middle and lower parts of the amorphous layer (Figs. 2f and A.8). The np-Fe^0 particles were smaller in the vapor and subsolidus layers than in the amorphous layer. The formation of np-Fe^0 particles was also accompanied by the redistribution of local elements. The Fe concentrated in np-Fe^0 particles and migrated into the amorphous layer, leaving an Mg-enriched signature in the subsolidus layer (Figs. 2i,j).

The sizes of the np-Fe^0 particles positively correlated with the Fa# values of olivine and the irradiation energy levels (Fig. 5). In Fa_{29}, the median size of np-Fe^0 increased from 4.4 ± 1.1 nm under P5mJ conditions to 10.0 ± 3.5 nm under M150mJ conditions (Figs. 5a–e). Similarly, in Fa_{50} and Fa_{71}, the median size of the np-Fe^0 particles increased from 12.4 ± 2.2 nm to 17.2 ± 3.6 nm and 14.8 ± 2.9 nm to 17.2 ± 7.5 nm, respectively, with increasing irradiation energy (Figs. 5f–j; 5k–o). The largest np-Fe^0 particles were produced by Fa_{100}, and the median size increased from 25.0 ± 5.0 nm to 33.8 ± 6.8 nm with increasing energy (Figs. 5p–t). Across all the energy levels examined, the np-Fe^0 particles were less than 30 nm in Fa_{29}, and they ranged from 6 nm to 40 nm in Fa_{50}, 8 nm to 47 nm in Fa_{71}, and from 10 nm to 55 nm in Fa_{100}. For each type of olivine, the np-Fe^0 size distribution pattern changed from a right-skewed distribution to a normal distribution, with the tendency shifting to a left-skewed distribution with increasing irradiation energy levels (Fig. 5). Such a distribution is consistent with the Ostwald ripening process that describes the nanoparticle growth process (Gommes 2019; Thompson et al. 2017). In addition, higher single-shot energy consistently produced larger np-Fe^0 particles when compared to the P75mJ (5 mJ × 15) and M75mJ (15 mJ × 5)

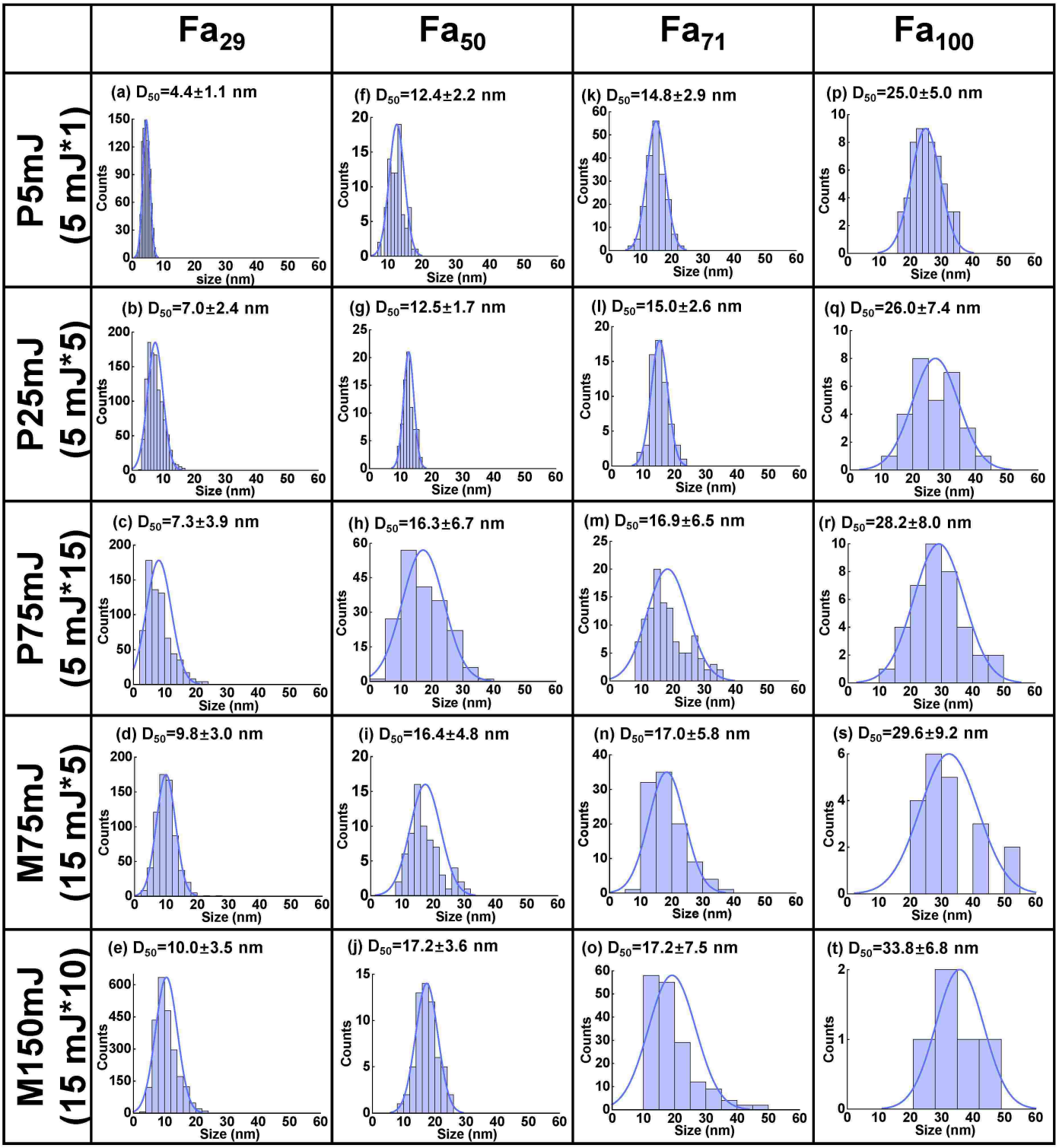

Fig. 5. Particle size distribution of np-Fe^0 in different types of olivine and under different irradiation energy levels. The particle size labeled in each subfigure was the median particle size. Images (a)–(e) are Fa_{29}, (f)–(j) are Fa_{50}, (k)–(o) are Fa_{71}, and (p)–(u) are Fa_{100}. The numbers of np-Fe^0 particles are negatively correlated with and the np-Fe^0 particle sizes are positively correlated with increasing Fe content and irradiation energy.

conditions (Fig. 5, images c, d, h, i, m, n, r, s). As the np-Fe^0 particles became larger, the shape of the nanoparticle changed from spherical to subangular (Fig. A.9). For comparison, the number of np-Fe^0 particles negatively correlated with the Fa# values, and the amounts of np-Fe^0 particles in different types of olivine were in the order of $Fa_{29} > Fa_{50} \approx Fa_{71} > Fa_{100}$ (Fig. 5).

The size-quantity distribution of the np-Fe^0 particles showed a tendency to increase in size but decrease in quantity with increasing irradiation energy levels and Fa# values. In our experiments, Fa_{29} under the lowest irradiation energy would produce the most abundant but smallest np-Fe^0 particles, and Fa_{100} under the highest irradiation energy would produce the least abundant

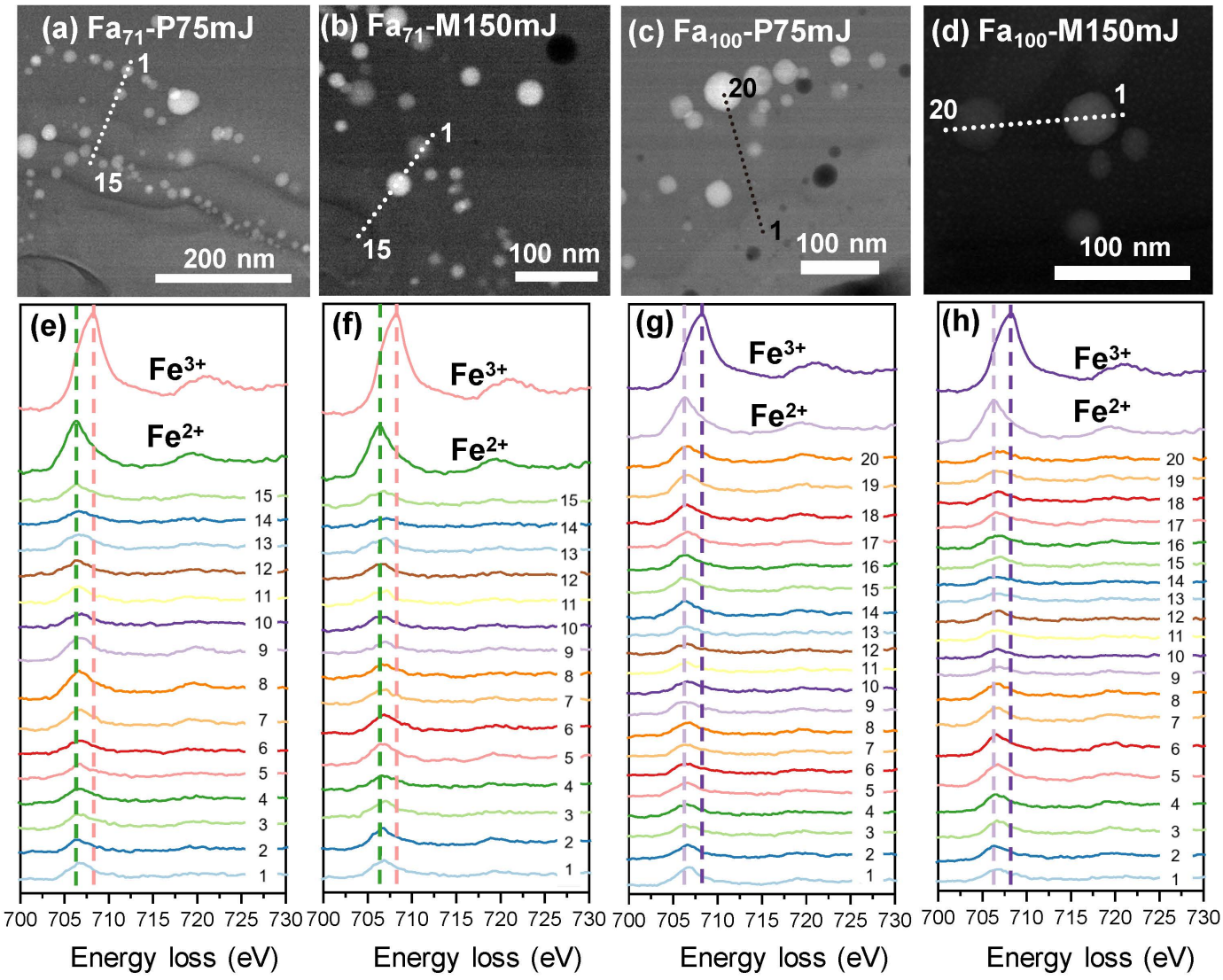

Fig. 6. TEM-EELS line scan analysis and the corresponding spectrum results of Fa_{71}-P75mJ, Fa_{71}-M150mJ, Fa_{100}-P75mJ, and Fa_{100}-M150mJ samples. Twenty points were sampled on Fa_{71}-P75mJ and Fa_{71}-M150mJ samples, and fifteen points were sampled for Fa_{100}-P75mJ and Fa_{100}-M150mJ samples. Analysis points of the samples are shown in the top row, and the corresponding Fe $L_{3,2}$ TEM-EELS data for samples and standard references are shown in the bottom row. Images (a) and (e) Fa_{71}-P75mJ; (b) and (f) Fa_{71}-M150mJ; (c) and (g) Fa_{100}-P75mJ; (d) and (h) Fa_{100}-M150mJ. The standard references show that Fe^{2+} and Fe^{3+} have distinct edge shapes and peak positions at 706.2 eV and 708 eV, respectively. The TEM-EELS line scan shows that the Fe in olivine and the matrix existed as Fe^{2+}, and no evidence of Fe^{3+} was found.

but most extensive np-Fe^0 particles (Fig. 5). These trends are consistent with previous laser irradiation experiments in which np-Fe^0 particles produced by San Carlos olivine (Fa_{09}) are mostly a few nanometers in size, which is smaller than those produced in Fa_{29} under similar irradiation energy conditions (Loeffler et al. 2016; Weber et al. 2020; Yang et al. 2017).

3.5. Formation mechanisms of np-Fe^0 particles in Fe-rich olivine

The proposed formation mechanisms of np-Fe^0 particles relevant to micrometeoroid impacts on olivine include vapor deposition of elemental iron (Sasaki et al. 2001), decomposition (Guo et al. 2022), and disproportionation (Li et al. 2022). In this study, with Fe-rich olivine under various energy conditions, we observed vapor-deposited np-Fe^0 particles originating in the outermost vapor deposition layer and decomposition-originated np-Fe^0 particles in the amorphous and subsolidus layers. The two types of np-Fe^0 particles can be visually distinguished.

The disproportionate origin of np-Fe^0 particles was not observed in our experiment. The TEM-EELS line scan analyzed four laser-irradiated samples, including Fa_{71}-P75mJ, Fa_{71}-M150mJ, Fa_{100}-P75mJ, and Fa_{100}-M150mJ, which represent Fa-dominant olivine being space weathered at locations for Phobos and the Moon, respectively. The TEM-EELS analysis also included a linear scan through the np-Fe^0, amorphous matrix, and crystalline olivine host for each sample. When comparing the TEM-EELS measurement data with the standard reference, we found that Fe in the amorphous matrix and crystalline olivine host existed as Fe^{2+} (Figs. 6e–h). No Fe^{3+} was found in the amorphous matrix surrounding the np-Fe^0.

The reason for the absence of disproportionation could not be determined in the current study. An essential factor suggested for the Fe disproportionation observed in the CE-5-returned lunar regolith is impact-induced high pressure during micrometeorite

impacts (Li et al. 2022; Mo et al. 2022) , which is not simulated by our laser irradiation experiments. We inferred that the high pressure or continuous heating required for Fe disproportionation cannot be achieved in our experimental settings. It is unclear whether the temperature needed for Fe disproportionation in fayalite would be lower than that in forsterite.

The presence of vapor-deposited np-Fe^0 and in situ-decomposed np-Fe^0 is primarily controlled by the olivine type and irradiation energy conditions, which ultimately relate to the instantaneous temperature of laser irradiation and the melting points of the target olivine. The np-Fe^0 particles formed via in situ decomposition were ubiquitously present in the amorphous and subsolidus layers. In particular, the subsolidus layer represents a transition state between the solid and liquid phases, suggesting that the thermal effects transferred from impact to this layer have diminished but still reach the conditions for np-Fe^0 production. The initially formed particles in the subsolidus layer are small (a few nanometers), and continuous heating allows large nanoparticles to grow at the expense of smaller nanoparticles. With increasing distance from the olivine host, np-Fe^0 particles grow gradually in size, suggesting slower cooling as an effect of thermal diffusivity (Weber et al. 2020). Under the same irradiation energy, the lower melting point of fayalite (1250 °C) compared to forsterite (1890 °C) would allow a longer time for np-Fe^0 to grow, and the higher Fe content in fayalitic olivine would provide sufficient Fe for the formation of np-Fe^0 particles. Therefore, with the increasing Fa# values of the initial olivine, the growing supply of Fe and the low melting point of olivine would facilitate the formation of large np-Fe^0 via olivine decomposition. It thus can be extrapolated that other Fe-rich minerals with low melting points may be able to produce large np-Fe^0 as the Fe-rich olivine did during the space weathering processes. Previous laser irradiation experiments have consistently demonstrated that targets such as ilmenite (melting point 1050 °C) and kamacite (melting point 800–900 °C) produce large np-Fe^0, similar to the Fe-rich olivine observed in this study (Wu et al. 2017).

We found only a few cases of vapor-deposited np-Fe^0 in our experiments, such as in Fa_{29} under almost all energy conditions, except for the highest energy level (M150mJ), and in Fa_{100} under the lowest irradiation energy conditions (P5mJ and P25mJ). Vapor-deposited np-Fe^0 can be largely absent in Fa-dominant olivine regardless of the energy levels and absent in Fo-dominant olivine under high irradiation energy. The formation of vapor-deposited np-Fe^0 may be primarily controlled by the instantaneous temperature during irradiation and may also be related to the melting point of olivine and the vaporization temperature of Fe. For Fo-dominant olivine, when the melting point is relatively higher than that of Fa-dominant olivine, the np-Fe^0 particles can condense from the vaporized materials under most energy conditions, except for the highest energy condition. For the fayalite, which has the lowest melting point of all the Fo–Fa solid solutions, the laser irradiation should produce substantially low instantaneous T under P5mJ conditions versus those under P75mJ conditions. High instantaneous T might account for the absence of vapor-deposited np-Fe^0 particles that Fe can vaporize and escape into the vacuum from the surface in our experiments. The lack of vapor-deposited np-Fe^0 and a low vapor-melt production ratio in Fa_{09} olivine under 15 mJ × 20 conditions have been inferred to potentially be due to the instantaneous T of ~7000 K (Weber et al. 2020).

Integrating the microscopic features of the laser alteration layer and np-Fe^0 particles, we suggest that Fo-dominant (Fa# < 50) and Fa-dominant (Fa# ⩾ 50) olivine may demonstrate distinct characteristics during thermal alteration induced by micrometeoroid impacts. Under the same impact flux and time, the Fa-dominant olivine would produce thicker altered rims (micron level) and grow larger np-Fe^0 particles (e.g., a substantial fraction of sizes >10 nm or even >40 nm) compared to the Fo-dominant olivine.

3.6. Near-infrared reflectance spectra of altered olivine

With increasing Fa# values of olivine, the NIR reflectance spectra of initial olivine decrease in albedo, and the 1000 nm absorption feature (R_{1000}) shifts to longer wavelengths with increasing Fa# values (Fig. A.10), consistent with previous observations (Dyar et al. 2009; Pinet et al. 2022). After laser irradiation, the NIR spectra of olivine samples (Fa_{29}, Fa_{50}, Fa_{71}, and Fa_{100}) under different conditions were compared (see Fig. 7). We used the absolute reflectance at 1900 nm (R_{1900}) to characterize the darkening effects in the NIR band, the ratio of reflectance at 2400 nm to 1900 nm (R_{2400}/R_{1900}) to characterize the reddening effect, and the band depth at 1000 nm (BD_{1000}) to describe the decrease in absorption (Table 2). The changes in spectral parameters relative to the initial olivine under different irradiation conditions are also listed in Table 2 to quantitatively compare the extent of spectral alteration effects in these different parameters.

For Fa_{29}, Fa_{50} and Fa_{71}, the NIR spectra of altered olivine exhibited a progressive spectral change with increasing irradiation energy under conditions simulating Phobos and the Moon, respectively (Figs. 7a,b,c,e,f,g). The irradiated olivine samples demonstrate a decrease in absolute reflectance (darkening), an increase in R_{2400}/R_{1900} slope (reddening), and attenuation in BD_{1000} (flattening). We note that Fa_{50} under M75mJ and M150mJ conditions showed similar reddening levels and thus no further reddening at higher energies. Comparing Fa_{29} to Fa_{71} olivine under P75mJ versus M75mJ conditions, the absolute reflectance R_{1900} and BD_{1000} under M75mJ are always higher than those under P75mJ, but the slopes of R_{2400}/R_{1900} are slightly lower under M75mJ than under P75mJ (Table 2). This indicates that under the same total irradiation energy, for Fa_{29}, Fa_{50}, and Fa_{71}, the spectra produced via high single-shot energy but with fewer shot times (15 mJ × 5) are relatively brighter but with a lower extent of reddening and feature attenuation compared to their counterparts under low single-shot energy but with more shot times (5 mJ × 15). Thus, we can conclude that both single-shot energy and total irradiation energy have essential effects on spectral modification, and caution needs to be taken when comparing spectral features across different single-shot irradiation conditions. In addition, the influence of Fa# values alone on the spectral parameters (i.e., darkening, reddening, feature attenuation) is relatively minor, and there is generally a lack of increasing or decreasing trends corresponding with increasing Fa# values (Fig. 8).

Pure fayalite (Fa_{100}) largely validates observations in Fa_{29} to Fa_{71} samples but demonstrates interesting exceptions (Figs. 7d,h; Table 2). From P5mJ to P75mJ, the reflectance spectra of Fa_{100} demonstrate progressive darkening and reddening and feature attenuation with increasing irradiation energy. While the band depth (BD_{1000}) continuously weakened under M75mJ and M150mJ conditions (reduced by 80.5% and 85.1%, respectively; Table 2), following the trend under Phobos conditions, the spectral parameters started to reverse from darkening and reddening to brightening and reddening (Figs. 7d,h; Table 2). Under M75mJ, the darkening and reddening effects were significantly weakened compared to the P75mJ condition. Under M150mJ, the absolute reflectance of R_{1900} was equivalent to the initial

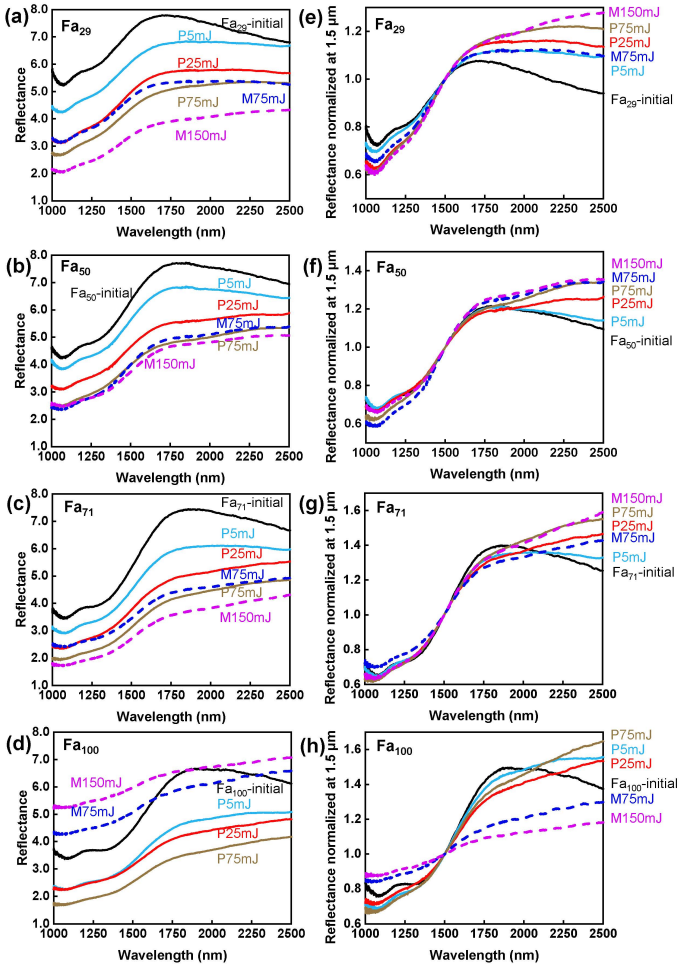

Fig. 7. NIR reflectance spectra of the Fe-rich olivine before and after laser irradiation in this study. The left column presents the NIR spectra of four types of Fe-rich olivine, and the right column presents the spectra but normalized at 1500 nm for comparison. Images (a) and (e) Fa_{29}; (b) and (f) Fa_{50}; (c) and (g) Fa_{71}; and (d) and (h) Fa_{100}. In each subfigure, the black solid line represents the spectra of the initial olivine; colored solid lines represent irradiated olivine simulating Phobos conditions, P5mJ (teal), P25mJ (red), and P75mJ (brown); colored dashed lines represent irradiated olivine simulating lunar conditions, M75mJ (blue) and M150mJ (purple). In general, most irradiated olivine samples demonstrate a decrease in reflectance (i.e., darkening) compared to the initial olivine and an increase in the R_{2400}/R_{1900} spectral slope (i.e., reddening). Exceptions occur in Fa_{50} and Fa_{100} under M75mJ and M150mJ conditions. Fa_{50} shows no further reddening under the M150mJ condition compared to that under the M75mJ condition. Fa_{100} shows an inversed pattern, with an increase in reflectance (i.e., brightening) and a lower extent of reddening under M75mJ and M150mJ conditions compared to those under P5mJ to P75mJ conditions. Attenuation of absorption occurred in all the irradiated samples.

olivine, and the R_{2400}/R_{1900} slope further decreased compared to that of the M75mJ condition, resulting in brightening and reddening under the most irradiated condition.

Almost all irradiated olivine samples demonstrated darkening and reddening spectral effects, of which darkening was the primary effect relative to reddening in the NIR band (Table 2). The only sample that demonstrated comparable darkening (10.5%) and reddening (8.1%) effects is Fa_{29}-P5mJ. In this particular sample, the np-Fe^0 particles have a median size of 4.4 nm ± 1.1 nm, without grains larger than 10 nm (Fig. 5a). In contrast, all the other samples contain substantial fractions of np-Fe^0 in the range of 10–40 nm or even larger (40–60 nm). We find the observations of np-Fe^0 fractions in the samples and the corresponding spectral alteration are consistent with those inferred by previous studies in the visible and NIR band, namely, the smallest size fraction (np-Fe^0 < 10 nm) controls reddening, the largest size fraction (np-Fe^0 > 40 nm) mainly results in darkening without reddening, and the intermediate size fraction (10–40 nm) has unique control over darkening or reddening based on the increasing iron concentration (see e.g., Cloutis et al. 2015; Kohout et al. 2014; Loeffler et al. 2016; Noble et al. 2007). Furthermore, increasing the volume fraction of the np-Fe^0 can also contribute to the darkening and reddening of the spectra and the weakening of the absorption bands. We suggest that in our Fe-rich olivine samples, a proportional increase in intermediate and large size fractions and an increase in the volume fraction of np-Fe^0 are likely to present and substantially contribute to the darkening of the spectra over the mostly reddening effect found in magnesian olivine (see e.g., Yamada et al. 1999; Hapke 2001). In addition, saturation of the space weathering effects is suggested for np-Fe^0 volume fractions ⩾1%, as the spectrum flattens with very low reflectance (Escobar-Cerezo et al. 2018). In comparison, our maximum feature attenuation reached 85.1% under the Fa_{100}-M150mJ condition and did not reach the saturation states of space weathering effects.

The brightening spectral feature produced by space-weathered olivine has not been reported previously in any simulation experiments via pulsed laser bombardment, ion implantation, or simply heating. In particular, the reversal from darkening and reddening (under P25mJ to P75mJ) to brightening and reddening (under M75mJ and M15mJ) in Fa_{100} in our experiments suggests that the irradiation energy (total energy and/or single-shot energy) and the Fe content in the initial olivine (fayalitic or Fe-dominant olivine) should be the key elements accounting for such unique spectral change. Because our synthetic olivine samples are relatively pure and the np-Fe^0 particles and laser alteration layers are the two primary space-weathered features, we infer that the substantial increase in thickness of the laser-altered layers on the fayalitic olivine may be critical, as the np-Fe^0 particles are known to produce darkening and reddening primarily in the NIR band. In Fa_{29}, Fa_{50}, and Fa_{71}, the thickness of altered layers is always less than 1 μm (maximum 916.3 nm). In comparison, the altered layers of Fa_{100} are mainly thicker than 1 μm, and they increase from 340.3 nm (P5mJ) to 1044.2 nm (P25mJ), 1429.3 nm (M75mJ), and 1697.0 nm (M150mJ). Although previous studies concluded that amorphization of mineral surfaces (in a few hundred nanometers) would lead to an overall darkening of the reflection spectra in the UV-Vis-NIR range even without considering np-Fe^0 (Zhang et al. 2022), as demonstrated in our experiments, when the altered glassy and amorphous rims became thick enough (>1 μm or >1.4 μm) and approached the wavelength of the infrared spectrum, they would substantially contribute to the spectral effects in the NIR band. The thickening alteration layers are composed of amorphous and subsolidus layers, and the np-Fe^0 particles increasing in size and volume reside within these layers. We infer that the substantially thick altered rims might effectively compensate for the darkening effects caused by the increasing size and volume of the np-Fe^0 particles, leaving reddening as the primary spectral effect in the sample. The thick alteration layers may also interfere by reducing the extent of the reddening effect. Depending on the relative contribution of the alteration layer thickness and np-Fe^0 particles, one can anticipate the spectral alteration from darkening and reddening to brightening and reddening in the Fe-rich olivine samples. Nevertheless, whether the spectra turn dark or bright,

Table 2. NIR spectral parameters of Fe-rich olivine before and after laser irradiation.

Samples	Absolute reflectance (R_{1900})	Changes relative to initial olivine	Slope (R_{2400}/R_{1900})	Changes relative to initial olivine	Band depth (BD_{1000})	Changes relative to initial olivine
Fa_{29}-initial	7.630	–	0.905	–	0.092	–
Fa_{29}-P5mJ	6.827	–10.5%	0.978	8.1%	0.046	–50.0%
Fa_{29}-P25mJ	5.778	–24.3%	0.987	9.1%	0.048	–47.8%
Fa_{29}-P75mJ	5.200	–31.8%	1.024	13.1%	0.033	–64.1%
Fa_{29}-M75mJ	5.354	–29.8%	0.990	9.4%	0.049	–46.7%
Fa_{29}-M150mJ	4.007	–47.5%	1.075	18.8%	0.046	–50.0%
Fa_{50}-initial	7.655	–	0.927	–	0.091	–
Fa_{50}-P5mJ	6.794	–11.2%	0.953	2.8%	0.089	–2.2%
Fa_{50}-P25mJ	5.605	–26.8%	1.038	12.0%	0.033	–63.7%
Fa_{50}-P75mJ	4.907	–35.9%	1.086	17.2%	0.030	–67.0%
Fa_{50}-M75mJ	5.030	–34.3%	1.066	15.0%	0.034	–62.6%
Fa_{50}-M150mJ	4.756	–37.9%	1.064	14.8%	0.044	–51.6%
Fa_{71}-initial	7.428	–	0.923	–	0.103	–
Fa_{71}-P5mJ	6.067	–18.3%	0.987	6.9%	0.073	–29.1%
Fa_{71}-P25mJ	5.069	–31.8%	1.076	16.6%	0.054	–47.6%
Fa_{71}-P75mJ	4.348	–41.5%	1.108	20.0%	0.025	–75.7%
Fa_{71}-M75mJ	4.548	–38.8%	1.074	16.4%	0.047	–54.4%
Fa_{71}-M150mJ	3.747	–49.6%	1.122	21.6%	0.049	–52.4%
Fa_{100}-initial	6.648	–	0.944	–	0.087	–
Fa_{100}-P5mJ	4.762	–28.4%	1.062	12.5%	0.055	–36.8%
Fa_{100}-P25mJ	4,313	–35.1%	1.103	16.8%	0.039	–55.2%
Fa_{100}-P75mJ	3.584	–46.1%	1.146	21.4%	0.034	–60.9%
Fa_{100}-M75mJ	6.036	–9.2%	1.081	14.5%	0.017	–80.5%
Fa_{100}-M150mJ	6.645	0.0%	1.057	12.0%	0.013	–85.1%

the band depth of absorption gradually weakens with increasing irradiation energy, contributing to flattening in the spectral features.

We note that the single-shot and total energy conditions selected to simulate those of Phobos and the Moon in our experiments are conservative and considered to simulate low to medium degrees of space weathering (as defined in Zhang et al. 2022), and higher energy conditions are expected to occur on both Phobos and the Moon. For instance, considering a higher impact velocity (e.g., 12 km s^{-1}; Table 1) and longer irradiation history (e.g., 4 Ga), a single-shot energy at 7 mJ and total energy at 178 mJ can be adopted for Phobos, which is higher than the present M150mJ conditions. Therefore, further investigation is required to determine whether the brightening and reduction in reddening found in Fa_{100} under M75mJ and M150mJ can be extrapolated for at least fayalitic olivine under medium or high degrees of space weathering or if such features occur in other Fe-dominant olivine (Fa# > 50).

3.7. Raman spectral characteristics of altered olivine

The Raman spectra of each olivine type before and after laser irradiation are compared in Fig. 9. The initial olivine samples showed typical double peaks between 800 and 900 cm^{-1}. The positions of the double peaks shifted toward lower wavenumbers with increasing Fa# values, that is, from Fa_{29} to Fa_{100}. The wavenumbers of doublet peak #1 (DB1) decreased from 821 to 815 cm^{-1}, and those of doublet peak #2 (DB2) decreased from 851 to 833 cm^{-1}. In addition, the intensity of DB2 gradually decreased and appeared as a shoulder beside the DB1 peak with increasing Fa# values, consistent with previous studies (Kuebler et al. 2006). After laser irradiation, the wavenumber, shape, and FWHM of the doublet peaks did not change substantially (Table A.3). The newly formed np-Fe^0 particles are pure metallic iron that have no Raman effects, and the potential reduction of the fluorescence-dominated background due to the formation of np-Fe^0 may facilitate a better interpretation of the individual mineral peaks by the Raman spectrometer (Weber et al. 2021, 2022). Amorphization of the olivine surface may cause local disorder and result in the broadening of Raman peaks, as suggested in previous studies (Rouquette et al. 2008; Santamaria-Perez et al. 2016); however, the amorphous layer showed no substantial influence in our experiments. The spectral intensities were significantly reduced by laser irradiation, and the extent of reduction showed no difference under different energy conditions (i.e., P75mJ vs. M150mJ; Fig. 9). Therefore, a lack of changes in the characteristic DB1 and DB2 after laser irradiation may allow for the identification and extraction of olivine Fo-Fa compositions, as was done for fresh olivine before space weathering (Kuebler et al. 2006).

In this experiment, we measured Raman spectra before and after laser irradiation only at room temperature. Previous studies suggested that below 150 K, forsterite may show negligible temperature-related shifts but that fayalite would show temperature-dependent changes in the lattice modes and modification of Raman spectra at low Stokes frequencies, potentially due to the high amount of iron in the mineral structures (Weber et al. 2014). Since Raman spectroscopy has been proposed for in situ investigations of airless celestial bodies, such as Phobos and the Moon (Usui et al. 2020), how to accurately constrain the Fo–Fa compositions under low temperature, particularly for space-weathered Fe-rich olivine, requires further study.

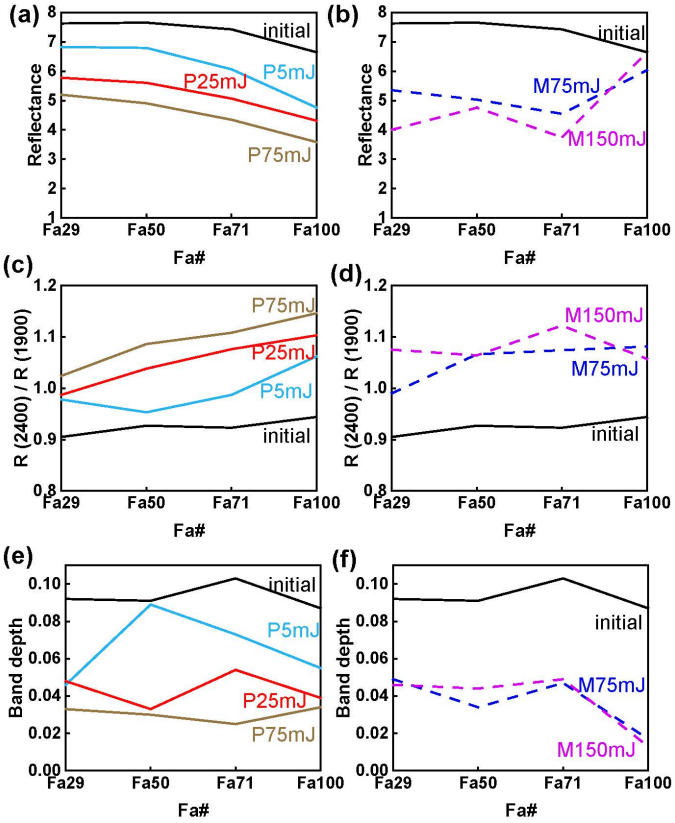

Fig. 8. Variations in NIR spectral parameters with increasing Fa# values of olivine under different irradiation energy conditions. Images (a) and (b) R_{1900}; (c) and (d) R_{2400}/R_{1900}; (e) and (f) BD_{1000}. The initial olivine is shown in black. Images (a), (c), and (e) show irradiations simulating Phobos conditions, P5mJ (teal line), P25mJ (red line), and P75mJ (brown line). Images (b), (d), and (f) show irradiations simulating Moon conditions, M75mJ (blue dashed line) and M150mJ (purple dashed line). Under Phobos conditions, the decrease in reflectance and increase in R_{2400}/R_{1900} spectral slope are approximately parallel to the initial olivine with increasing Fa# values. Variations in band depth occured in different Fa# samples, but overall the band depth attenuated after irradiations. Under the Moon conditions, the changes in reflectance, R_{2400}/R_{1900} spectral slope change, and band depth generally followed the trends of initial olivine, with exceptions in Fa_{100}-M75mJ and -M150mJ.

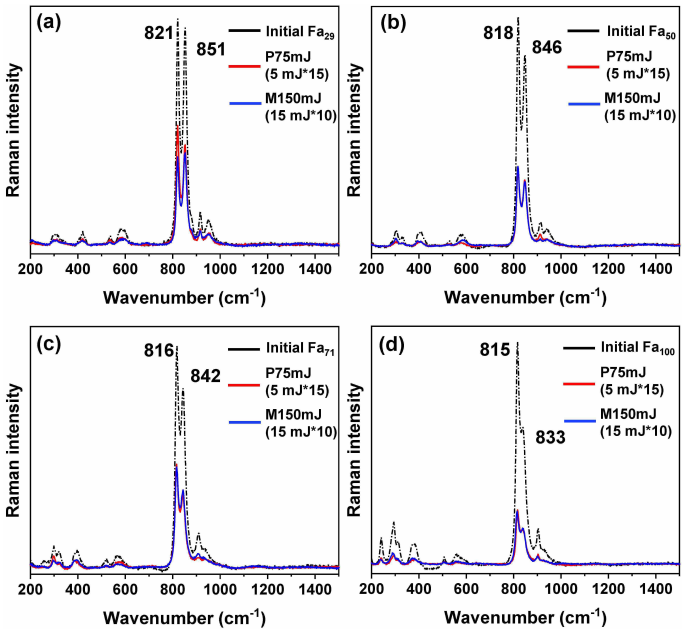

Fig. 9. Raman spectra before and after laser irradiations of the Fe-rich olivine. Image (a) Fa_{29}, (b) Fa_{50}, (c) Fa_{71}, and (d) Fa_{100}. Spectra in black are the Raman spectra of initial olivine before laser irradiation. The spectra in red and blue represent irradiation conditions of P75mJ and M150mJ, respectively. The initial olivine samples showed typical double peaks between 800 and 900 cm^{-1}, and the positions of the double peaks shifted toward lower wavenumbers with increasing Fa# values. From Fa_{29} to Fa_{100}, the wavenumbers of doublet peak #1 (DB1) decreased from 821 to 815 cm^{-1}, and those of doublet peak #2 (DB2) decreased from 851 to 833 cm^{-1}. The intensity of DB2 gradually decreased and appeared as a shoulder beside the DB1 peak with increasing Fa# value in initial olivine. After laser irradiation, the wavenumber, shape, and FWHM of the doublet peaks did not change substantially. The spectral intensities were greatly reduced by laser irradiation, and the extent of reduction showed no difference under different energy conditions.

4. Implications

The simulation experiments in this study mainly account for the thermal effects of micrometeoroid impacts on olivine; thus, cautions should be taken when comparing our findings with space weathering phenomena in natural samples that have experienced multiple processes and have complex weathering histories. In addition, in natural space-weathered materials, solar wind irradiation can cause faster, significant spectral change at a timescale of 10^4–10^6 yr, compared to 10^8–10^9 yr for micrometeoroid bombardment (Noguchi et al. 2011; Sasaki et al. 2001). Nevertheless, our experiments suggest that when subjected to micrometeoroid impacts on the lunar surface, fayalitic olivine responds faster to space weathering than magnesian olivine. For Fo-dominant olivine (e.g., Fa_{29}), np-Fe^0 formed via vapor deposition and in situ decomposition are both present, primarily in the size of <10 nm. Larger np-Fe^0 particles (10–30 nm) may also form in the amorphous layer during prolonged space weathering. For Fa-dominant olivine (Fa# ⩾ 50), np-Fe^0 particles mainly formed via olivine decomposition and produced large np-Fe^0 particles (generally >10 nm; substantial fraction >40 nm).

Similar to what was observed with Apollo samples, Mg-rich olivine (e.g., Fa_{10}) mainly produced vapor-deposited np-Fe^0 (a few nanometers in size) during micrometeoroid impacts (Noble et al. 2005; Pieters & Noble 2016). Therefore, other processes would be required to produce larger np-Fe^0 particles (tens of nanometers in size), such as impacts and gardening (e.g., in forming agglutinitic glass), solar wind ion irradiation, and friction between particles. In contrast, in the Fa-dominant or fayalitic olivine in the lunar regolith, a thick altered rim and large np-Fe^0 particles 40–50 nm formed directly via olivine decomposition can be expected. Since fayalitic olivine is more susceptible to thermal alteration than Mg-rich olivine, processes other than impact-induced thermal effects may also produce large np-Fe^0 particles, such as heating induced via friction. This supports that the np-Fe^0 particles on fayalitic olivine (Fa# ⩾ 85) in the CE-5 lunar samples are not generated by micrometeoroid impacts; otherwise, a much thicker alteration rim would be expected to be present. The micrometeoroid impact effects on younger CE-5 lunar regolith during exposure (less than 100 Ma) should be relatively low, and the grains did not experience extensive heating events after exposure to the lunar surface (Guo et al. 2022).

For Phobos, the striking blue-red contrast on the surface is due to compositional variations or spatial variations in its physical surface properties (Ballouz et al. 2019; Rosenblatt 2011). A 0.65 μm absorption peak is present in the reddening region

of Phobos but absent in the blue regions, indicating a potential feature yielded via space weathering or possibly the presence of highly desiccated Fe-phyllosilicate minerals native to Phobos (Fraeman et al. 2014). In addition, metal-OH absorption peaks at 2.8 μm are present, originating through solar wind interactions with the weathering layer of the surface of Phobos (Fraeman et al. 2014). Regarding the origin hypotheses of Phobos, substantial olivine is expected to be present if Phobos had been captured from either organic-poor and water-poor outer Solar System bodies or inner Solar System bodies. Fe-rich olivine is still expected to be present if Phobos had been co-accreted with Mars or if it originated directly from Mars via giant impacts (Cho et al. 2021). Our experiments suggest that if the olivine on Phobos is Fe-rich or even Fa-dominant, which would be similar to the olivine widely present on the Martian surface (Koeppen & Hamilton 2008), space weathering by micrometeoroid impacts under various energy levels could produce dark and red units and bright and red units. If Phobos has been subjected to prolonged space weathering, such as ~4 Ga if Phobos originated via a giant impact that formed the Borealis basin (Citron et al. 2015), a larger fraction of >40 nm np-Fe^0 particles and thick alteration rims would be expected to be produced. While large np-Fe^0 particles (10–60 nm) alone may result in primary darkening with minor reddening effects on the Phobos surface, substantially thick alteration rims induced via medium to high degrees of space weathering may inversely brighten the weathered surfaces. If considering only albedo and spectral slope change in the NIR band, a fayalite-rich region that has been subjected to intensive space weathering might be mistakenly treated as a relatively less weathered region because it appears brighter and less red in the former case.

We note that the Phobos surface is not uniformly weathered, the solar wind irradiation flux is 15–100 times higher, and the meteoroid impact flux is four times higher at the front surface compared to those on the far side (Christou et al. 2021; Nénon et al. 2021). Therefore, intensive space weathering features, including the formation of large-sized np-Fe^0 particles and thick alteration rims, are expected on the front side, contributing to substantially altering the NIR spectra of the Phobos surface. In addition, compared to the Moon, the flux and speed of the micrometeoroid impacts and solar wind ions decline substantially at locations of Phobos and Deimos or further, making the compositions of olivine a more critical factor controlling the optical properties of surface materials than the external space weathering factors.

Finally, several macroscopic characteristics of the laser-irradiated Fe-rich olivine require further study, including the mid-infrared and magnetic characteristics and the quantitative inversion of the optical properties of laser-irradiated olivine samples. Further studies are needed to examine how the space-weathered Fe-rich olivine may further contribute to the spectral slope behavior of olivine-pyroxene mixtures (e.g., for Q- and S-type asteroids) on different timescales and how the solar wind and micrometeoroid bombardments and the superposition of the two effects would influence the spectra of Fe-rich olivine.

5. Conclusions

In this study, we conducted nanosecond pulsed laser irradiation experiments using a set of synthetic Fe-rich olivine samples (Fa_{29}, Fa_{50}, Fa_{71}, and Fa_{100}). Three energy levels (5 mJ × 1, 5 mJ × 5, and 5 mJ × 15) were examined to simulate the energy level of Phobos, and two energy levels (15 mJ × 5 and 15 mJ × 10) were examined to simulate the energy level of the Moon. The microscopic features and Raman spectra of space-weathered Fe-rich olivine were characterized in detail. The findings are summarized as follows:

1. The structure of laser alteration layers is primarily controlled by the irradiation energy and Fe content of olivine. The thickness of the layers roughly increases with irradiation energy. The laser alteration layer of Fa_{100} reached a micron-level thickness substantially thicker than those of Fo-Fa solid solution olivine;
2. The np-Fe^0 particles formed via in situ decomposition are ubiquitously present in all the Fe-rich olivine, and the np-Fe^0 particles formed by vapor deposition are primarily present in Fa_{29} and rarely found in Fa-dominant olivine (Fa# ⩾ 50). In the results from the laser irradiation experiment, we did not observe the disproportionate origin of np-Fe^0 particles;
3. The size-quantity distribution of np-Fe^0 particles showed a tendency to increase in size and decrease in quantity with increasing irradiation energy levels and Fa# values. As the Fa# values increase from Fa_{10} to Fe-rich (Fa_{29}) or Fa-dominant (Fa# ⩾ 50), intermediate (10–40 nm) and large (>40 nm) size fractions of np-Fe^0 proportionally increase, which may substantially contribute to darkening of the spectra over reddening, as found in magnesian olivine;
4. The NIR spectra of the space-weathered olivine turned dark and red in most cases, with primary darkening over minor reddening effects occurring due to the formation of large-sized and increasing-volume fractions of np-Fe^0 particles. Brightening and reduction in reddening of the NIR band were also found in Fa_{100} with increasing irradiation energies, potentially due to the spectral effects of micron-level thickness alteration layers superimposed on the large np-Fe^0 particles. In either case, the band depth of absorption gradually weakens with increasing irradiation energy, contributing to flattening of the spectral features;
5. The Raman spectra show a reduction in intensity but no peak shifts in the weathered olivine, allowing for identification and quantification of Fo–Fa compositions on an airless body;
6. The distance of Phobos and Deimos from the Sun makes the Fa# value of olivine a more critical factor in controlling the SWSAEs. If the Phobos is Fe-rich or even Fa-dominant, thick alteration rims and large np-Fe^0 particles (10–60 nm) formed via space weathering may cause darkening-reddening and potentially brightening-reddening spectral effects on the surface of Phobos and Deimos.

Our study demonstrates that the iron content of olivine is a key factor influencing the SWSAEs. Understanding how Fe-rich olivine or Fa-dominant olivine responds to a variety of space weathering processes can aid data interpretation when exploring airless bodies potentially bearing Fe-rich olivine, such as the Moon, Phobos and Deimos, and asteroids. As stated in the previous section, several macroscopic characteristics of the laser-irradiated Fe-rich olivine samples require further study, including the mid-infrared and magnetic characteristics and the quantitative inversion of the optical properties. Further studies are needed to examine how space-weathered Fe-rich olivine may further contribute to the spectral slope behavior of olivine-pyroxene mixtures (e.g., for Q- and S-type asteroids) on different timescales and how solar wind and micrometeoroid bombardments and the superposition of the two effects influence the spectra of Fe-rich olivine.

Acknowledgements. We are very grateful to Huapei Wang and Junxiang Miao for their help in the attempt to measure the magnetic signatures in the altered

olivine samples. We also greatly appreciate the reviewer Tomas Kohout and the editor Emmanuel Lellouch for their constructive suggestions to help us improve this manuscript. This work was supported by the B-type Strategic Priority Program of the Chinese Academy of Sciences (No. XDB41000000), Pre-research project on Civil Aerospace Technologies funded by China National Space Administration (CNSA) (No. D020102), Key Research Program of the Chinese Academy of Sciences (ZDBS-SSW-TLC001), Program of the Institute of Geology & Geophysics CAS (No.IGGCAS-201905), National Natural Science Foundation of China (Nos. 41573022 and 42203047), Key Project of Shaanxi Provincial Natural Science Basic Research Program (No. 2023-JC-ZD-16), Science and Technology Planning Project of Guangzhou (No. 202102021184), Innovation Training Program for College Students of Guangdong Province (No. S202111845208), Hong Kong Research Grants Council Research Impact Fund Project (No. R5043-19), The Key Research Program of Frontier Sciences, CAS (No. QYZDY-SSW-DQC028), Beijing Municipal Science and Technology Commission (No. Z181100002918003), Youth Innovation Promotion Association of CAS (Y201867), National Natural Science Foundation of China (41931077).

References

Bagheri, A., Khan, A., Efroimsky, M., Kruglyakov, M., & Giardini, D. 2021, Nat. Astron., 5, 539
Ballouz, R.-L., Baresi, N., Crites, S. T., Kawakatsu, Y., & Fujimoto, M. 2019, Nat. Geosci., 12, 229
Canup, R., & Salmon, J. 2018, Sci. Adv., 4, eaar6887
Cho, Y., Böttger, U., Rull, F., et al. 2021, Earth Planets Space, 73, 1
Chrbolkova, K., Brunetto, R., Durech, J., et al. 2021, A&A, 654, A143
Chrbolková, K., Halodová, P., Kohout, T., et al. 2022, A&A, 665, A14
Christou, A. A., Borisov, G., Dell'Oro, A., Cellino, A., & Devogèle, M. 2021, Icarus, 354, 113994
Citron, R. I., Genda, H., & Ida, S. 2015, Icarus, 252, 334
Cloutis, E. A., Sanchez, J. A., Reddy, V., et al. 2015, Icarus, 252, 39
Divine, N. 1993, J. Geophys. Res., 98, 17029
Du, W., Walker, D., Clark, S. M., Li, X., & Li, B. 2017, Am. Mineralogist, 102, 2307
Dyar, M., Sklute, E., Menzies, O., et al. 2009, Am. Mineralogist, 94, 883
Escobar-Cerezo, J., Penttilä, A., Kohout, T., et al. 2018, ApJ, 853, 71
Fazio, A., Harries, D., Matthäus, G., et al. 2018, Icarus, 299, 240
Fraeman, A., Arvidson, R., Murchie, S., et al. 2012, J. Geophys. Res.: Planets, 117
Fraeman, A. A., Murchie, S. L., Arvidson, R. E., et al. 2014, Icarus, 229, 196
Gommes, C. J. 2019, Nanoscale, 11, 7386
Grün, E., Fechtig, H., Hanner, M., et al. 1991, In-situ Exploration of Dust in the Solar System and Initial Results from the Galileo Dust Detector (Springer), 21
Guo, Z., Li, C., Li, Y., et al. 2022, Geophys. Res. Lett., 49, e2021GL097323
Hamann, C., Luther, R., Ebert, M., et al. 2016, Geophys. Res. Lett., 43, 10,602
Han, H.-J., Lu, X.-P., Yang, Y.-Z., Zhang, H., & Mutelo, A. M. 2020, Res. Astron. Astrophys., 20, 129
Hapke, B. 2001, J. Geophys. Res.: Planets, 106, 10039
Hyodo, R., Genda, H., Charnoz, S., & Rosenblatt, P. 2017, ApJ, 845, 125
Keller, L. P., & McKay, D. S. 1997, Geochim. Cosmochim. Acta, 61, 2331
Koeppen, W. C., & Hamilton, V. E. 2008, J. Geophys. Res.: Planets, 113
Kohout, T., Čuda, J., Filip, J., et al. 2014, Icarus, 237, 75
Kuebler, K. E., Jolliff, B. L., Wang, A., & Haskin, L. A. 2006, Geochim. Cosmochim. Acta, 70, 6201
Kuramoto, K., Kawakatsu, Y., Fujimoto, M., et al. 2022, Earth Planets Space, 74, 1
Li, C., Hu, H., Yang, M.-F., et al. 2021, Natl. Sci. Rev., 9, nwab188
Li, C., Guo, Z., Li, Y., et al. 2022, Nat. Astron., 6, 1156
Loeffler, M., Dukes, C., Christoffersen, R., & Baragiola, R. 2016, Meteor. Planet. Sci., 51, 261
Markley, M., & Kletetschka, G. 2016, Icarus, 268, 204
Miyamoto, H., Niihara, T., Wada, K., et al. 2021, Earth, Planets Space, 73, 1
Mo, B., Guo, Z., Li, Y., et al. 2022, Atomic Spectroscopy, 43, 53
Nénon, Q., Poppe, A. R., Rahmati, A., & McFadden, J. P. 2021, Nat. Geosci., 14, 61
Noble, S. K., Keller, L. P., & Pieters, C. M. 2005, Meteor. Planet. Sci., 40, 397
Noble, S. K., Pieters, C. M., & Keller, L. P. 2007, Icarus, 192, 629
Noguchi, T., Nakamura, T., Kimura, M., et al. 2011, Science, 333, 1121
Pieters, C. M., & Noble, S. K. 2016, J. Geophys. Res. Planets, 121, 1865
Pinet, P. C., Daydou, Y. H., & Chevrel, S. D. 2022, Icarus, 373, 114765
Qi, C., Zhao, Y., Zimmerman, M. E., Kim, D., & Kohlstedt, D. L. 2021, J. Geophys. Res.: Solid Earth, 126, e2020JB019629
Quadery, A. H., Pacheco, S., Au, A., et al. 2015, J. Geophys. Res.: Planets, 120, 643
Rosenblatt, P. 2011, A&ARv, 19, 1
Rouquette, J., Kantor, I., McCammon, C., Dmitriev, V., & Dubrovinsky, L. 2008, Inorg. Chem., 47, 2668
Santamaria-Perez, D., Thomson, A., Segura, A., et al. 2016, Am. Mineralogist, 101, 1642
Sasaki, S., Nakamura, K., Hamabe, Y., Kurahashi, E., & Hiroi, T. 2001, Nature, 410, 555
Sasaki, S., Hiroi, T., Nakamura, K., et al. 2002, Adv. Space Res., 29, 783
Shilobreeva, S., Zinenko, V., Agafonov, Y. A., Saraykin, V., & Bronsky, V. 2014, Geochem. Int., 52, 604
Thompson, M. S., Zega, T. J., & Howe, J. Y. 2017, Meteoritics & Planet. Sci., 52, 413
Usui, T., Bajo, K.-i., Fujiya, W., et al. 2020, Space Sci. Rev., 216
Vandemoortele, B., Reynard, B., Rochette, P., et al. 2007, Earth Planet. Sci. Lett., 262, 37
Wang, K., Moynier, F., Podosek, F. A., & Foriel, J. 2012, Earth Planet. Sci. Lett., 337–338, 17
Weber, I., Böttger, U., Pavlov, S., Jessberger, E., & Hübers, H.-W. 2014, Planet. Space Sci., 104, 163
Weber, I., Stojic, A. N., Morlok, A., et al. 2020, Earth Planet. Sci. Lett., 530
Weber, I., Reitze, M. P., Heeger, M., et al. 2021, Earth Planet. Sci. Lett., 569, 117072
Weber, I., Böttger, U., Hanke, F., et al. 2022, J. Raman Spectrosc., 53, 411
Wu, Y., Li, X., Yao, W., & Wang, S. 2017, J. Geophys. Res.: Planets, 122, 1956
Yamada, M., Sasaki, S., Nagahara, H., et al. 1999, Earth Planets Space, 51, 1255
Yang, Y., Zhang, H., Wang, Z., et al. 2017, A&A, 597, A50
Zhang, P., Tai, K., Li, Y., et al. 2022, A&A, 659, A78
Zhao, Y.-H., Zimmerman, M. E., & Kohlstedt, D. L. 2009, Earth Planet. Sci. Lett., 287, 229

Appendix A: Supplementary information

Table A.1. Compositions of synthetic Fe-rich olivine used in this study.

Fa#	FeO wt%	MgO wt%	SiO_2 wt%	Al_2O_3 wt%	CaO wt%	MnO wt%	Ni wt%
Fa_{100}	70.9	0.01	27.8	0.06	0.25	0.03	0.03
Fa_{71}	54.8	12.5	31.0	0.07	0.22	0.05	0.06
Fa_{50}	41.6	23.3	33.2	0.19	0.24	0.16	0.08
Fa_{29}	26.3	35.8	35.9	0.26	0.32	0.11	0.23

Notes. Fa# = $Fe_{mol}/(Fe_{mol}+Mg_{mol}) \times 100$

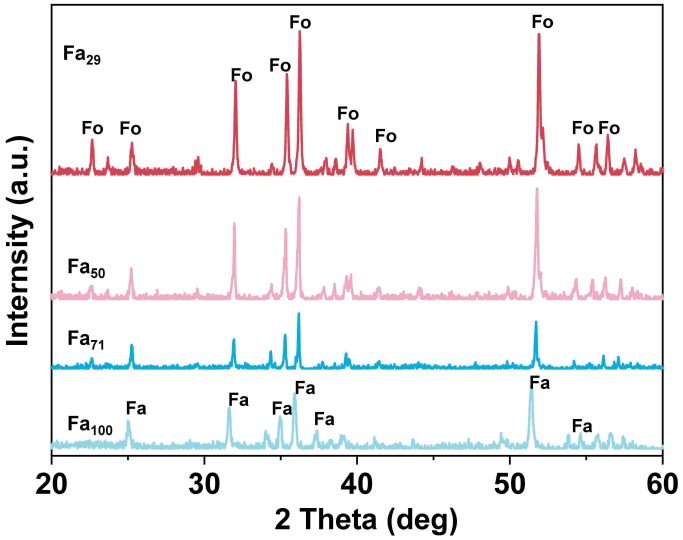

Fig. A.1. X-ray diffraction patterns of initial olivine with different Fe contents. The four types of olivine include Fa_{29}, Fa_{50}, Fa_{71}, and Fa_{100}. The corresponding peaks of fayalite and forsterite are marked in the Fa_{100} and Fa_{29} patterns, respectively.

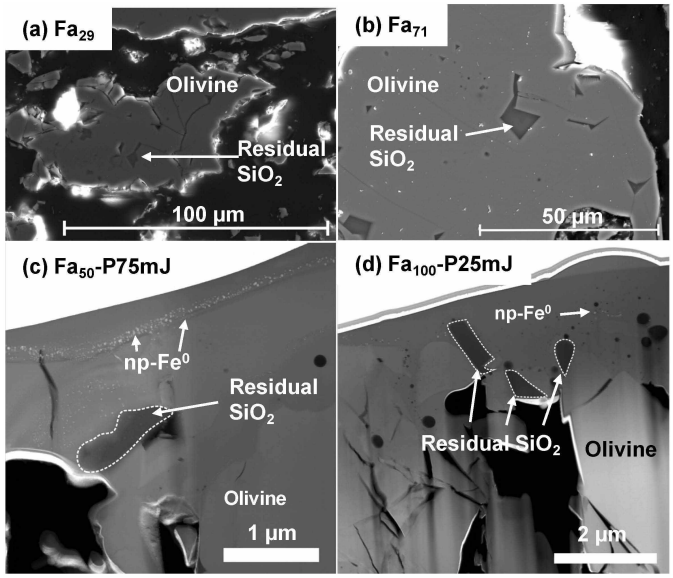

Fig. A.2. Residual SiO_2 identified in the cross sections of initial olivine grains and in the FIB foils of laser-irradiated olivine. Images (a) Fa_{29} and (b) Fa_{71} are the cross sections of initial olivine grains observed by SEM. The residual SiO_2 was embedded in the interior of the olivine and irregular in shape. The boundary between residual SiO_2 and olivine was clear. Images (c) Fa_{50}-P75mJ and (d) Fa_{100}-P25mJ are the FIB foils of laser-irradiated olivine samples. White dashed curves outline the altered residual SiO_2 present in part of the observed area by TEM. The residual SiO_2 affected by the laser irradiation showed amorphous morphologies with blurred boundaries with the matrix. The SEM-EDS analyses were conducted using an FEI Scios at 5 kV. The TEM-EDS analyses were performed using a Talos F200S at 200 kV.

Fig. A.3. Synthetic Fe-rich olivine powders before laser irradiation. The grain size of the powders is <75 μm. Image (a) Fa_{29}, (b) Fa_{50}, (c) Fa_{71}, and (d) Fa_{100}. The colors of the initial olivine gradually change from white to dark green with increasing Fe content.

Table A.2. Average thickness of the amorphous layer formed on the olivine rim under different irradiation energies. (Source data for plotting Fig. 4.)

Irradiation conditions	Amorphous layer thickness (nm)			
	Fa29	Fa50	Fa71	Fa100
P5mJ	193.5 ± 11.7	291.0 ± 23.6	322.8 ± 12.5	340.3 ± 19.7
P25mJ	430.6 ± 67.2	411.0 ± 74.6	430.6 ± 67.2	1044.2 ± 71.3
P75mJ	593.7 ± 82.3	447.2 ± 57.6	593.7 ± 82.3	1278.5 ± 85.5
M75mJ	781.4 ± 103.6	589.3 ± 78.6	709.4 ± 114.2	1429.3 ± 47.4
M150mJ	916.3 ± 176.8	620.4 ± 103.3	836.5 ± 143.6	1697.0 ± 82.6

Table A.3. Raman spectra of olivine before and after laser irradiation.

Samples	DB1		DB2	
	xc (cm^{-1})	FWHM (cm^{-1})	xc (cm^{-1})	FWHM (cm^{-1})
Fa_{100} (initial)	815.3±0.2	12.1±0.6	833.1±0.6	44.2±0.9
Fa_{100}-P75mJ	815.6±0.2	11.8±0.6	834.1±0.6	43.8±0.9
Fa_{100}-M150mJ	813.2±0.3	12.7±0.9	833.0±0.8	44.5±1.3
Fa_{71} (initial)	816.2±0.1	16.8±0.3	842.1±0.3	29.9±0.8
Fa_{71}-P75mJ	815.5±0.1	15.8±1.0	840.9±0.4	34.4±1.0
Fa_{71}-M150mJ	815.5±0.1	15.2±0.5	840.6±0.5	35.5±1.2
Fa_{50} (initial)	818.5±0.1	16.7±0.3	846.8±0.2	26.7±0.5
Fa_{50}-P75mJ	818.2±0.1	16.6±0.3	846.5±0.2	27.5±0.6
Fa_{50}-M150mJ	817.8±0.1	16.4±0.3	846.4±0.2	27.2±0.6
Fa_{29} (initial)	821.4±0.1	16.4±0.2	851.5±0.1	22.8±0.3
Fa_{29}-P75mJ	820.9±0.1	16.9±0.2	851.3±0.1	23.2±0.3
Fa_{29}-M150mJ	821.0±0.2	15.7±0.5	851.2±0.2	23.7±0.6

Notes. The FWHM and peak positions of the spectra were obtained by Gaussian fitting.

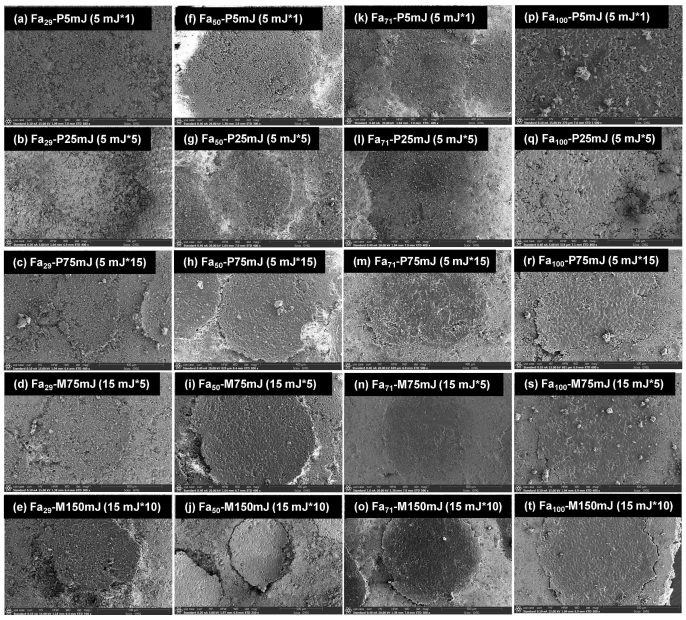

Fig. A.4. Secondary electron images of the laser-irradiated pits on the olivine pellets. Each column represents olivine with the same Fa# values. From left to right, Fa_{29}, Fa_{50}, Fa_{71}, and Fa_{100} are shown. Each row represents the same irradiation energy levels. From top to bottom, P5mJ, P25mJ, P75mJ, M75mJ, and M150mJ energy levels are shown.

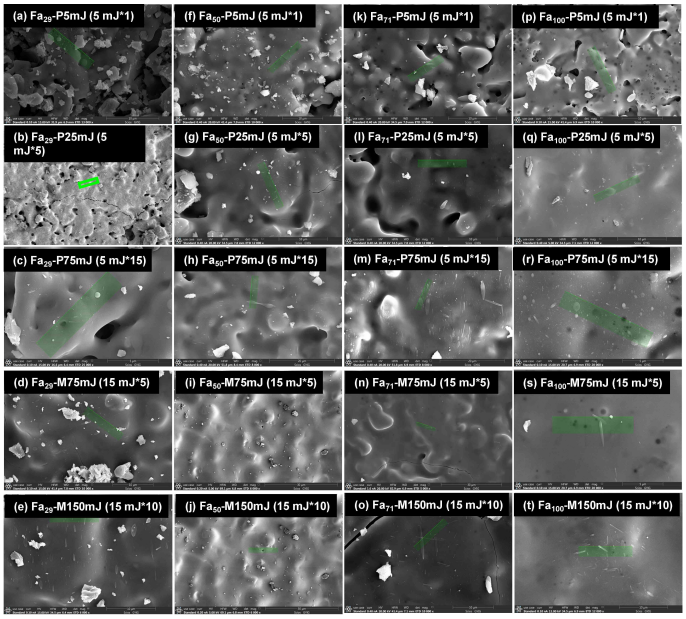

Fig. A.5. Secondary electron images showing the locations from which the FIB slices were extracted from the laser-irradiated pits on the olivine targets. The locations are shown in green boxes. Each column represents olivine with the same Fa# values. From left to right, Fa_{29}, Fa_{50}, Fa_{71}, and $Fa100_{100}$ are shown. Each row represents the same irradiation energy levels. From top to bottom, P5mJ, P25mJ, P75mJ, M75mJ, and M150mJ energy levels are shown.

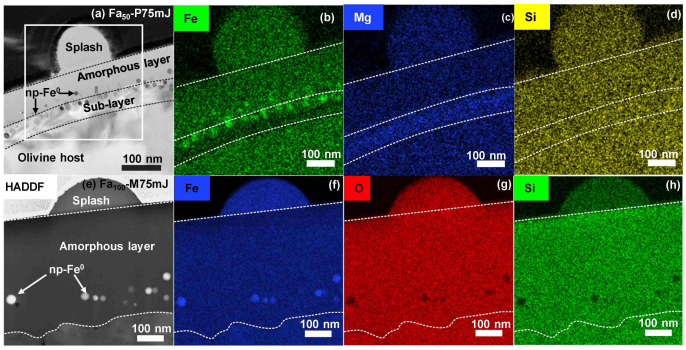

Fig. A.6. TEM analysis of the impact-induced splash materials deposited on the olivine surface showing two distinctive compositions. Image (a) shows bright-field TEM mapping of Fa_{50}-P75mJ with the splash materials and np-Fe^0 particles. Images (b)-(d) show the EDS mapping of Fe, Mg, and Si of the area highlighted by the white box in image (a). The splash material shares the same composition as the subsurface materials. Image (e) shows a high-angle annular dark-field (HAADF) TEM image of Fa_{100}-M75mJ with the splash and np-Fe^0 particles. Images (f)-(h) show the EDS mapping of Fe, O, and Si of the area in image (e). The splash material is Si-poor compared to the subsurface materials.

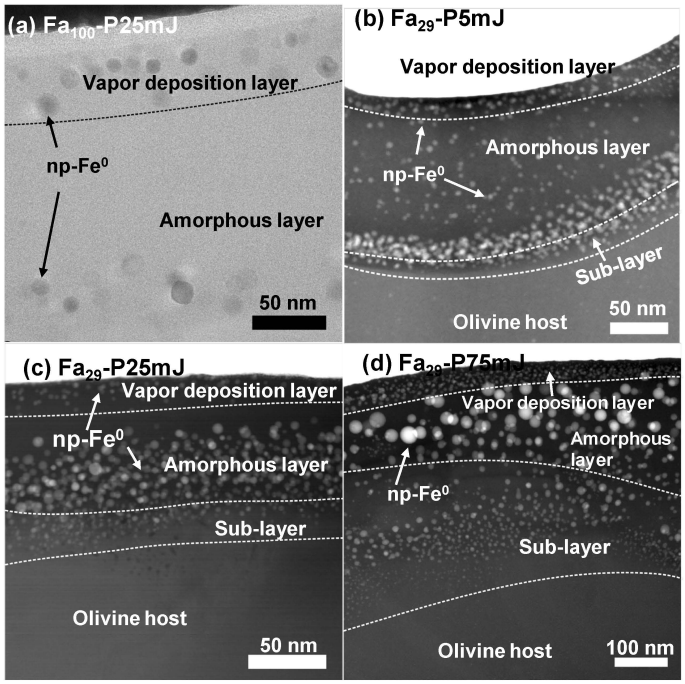

Fig. A.7. TEM images showing the np-Fe^0 particles within the vapor deposition layer. Image (a) Fa_{100}-P25mJ experiment, (b) Fa_{29}-P5mJ experiment, (c) Fa_{29}-P25mJ experiment, (d) Fa_{29}-P75mJ experiment, and (e) Fa_{29}-M75mJ experiment. The np-Fe^0 particles formed via vapor deposition were distinct in distribution and grain size compared to those in the middle and bottom of the amorphous layer. The former were evenly small and present close to the upper boundary of the vapor deposition layer, indicating different formation pathways from those in the amorphous and subsolidus layers.

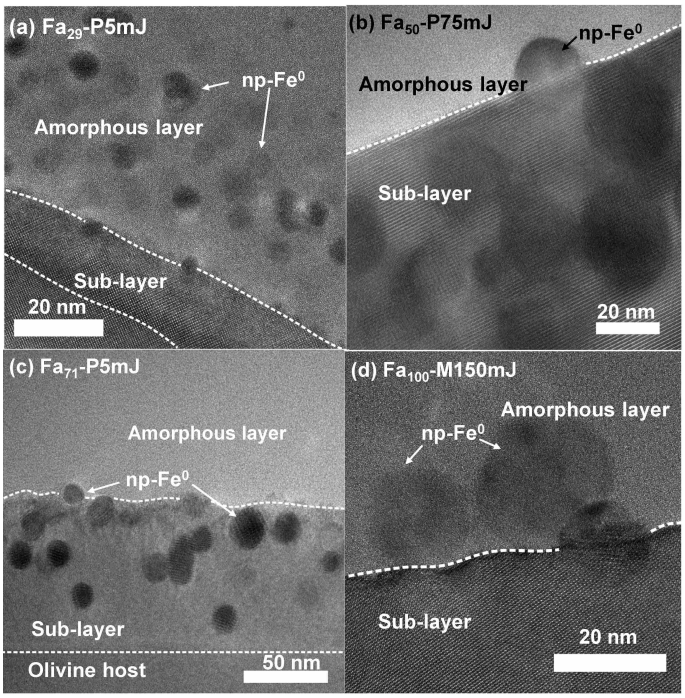

Fig. A.8. High-resolution TEM images showing the formation of np-Fe^0 particles in the subsolidus layer and migration into the amorphous layer. Image (a) Fa_{29}-P5mJ, (b) Fa_{50}-P75mJ, (c) Fa_{71}-P5mJ, and (d) Fa_{100}-M150mJ. The lattice fringes of olivine and newly formed np-Fe^0 particles can be observed.

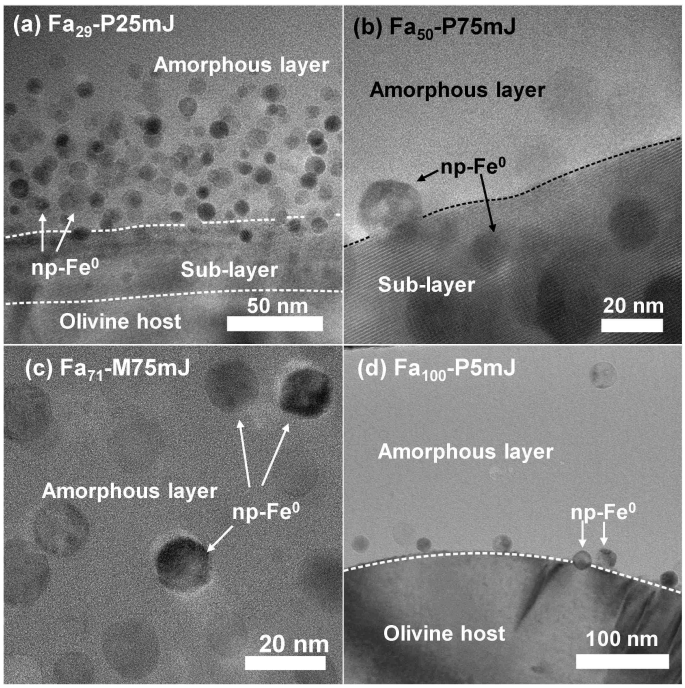

Fig. A.9. TEM images showing the different morphologies of the produced np-Fe^0 particles. Image (a) shows the Fa_{29}-P25mJ experiment produced generally spherical shapes of np-Fe^0 particles distributed in the subsolidus layer and at the bottom of the amorphous layer. Image (b) shows the Fa_{50}-P75mJ experiment produced angular and spherical-shaped npFe^0 particles dispersed in the subsolidus layer and at the bottom of the amorphous layer. Image (c) shows the Fa_{71}-M75mJ experiment had the most angular and subangular-shaped npFe^0 particles, with fewer spherical particles. Image (d) shows the Fa_{100}-P5mJ experiment commonly produced angular-shaped np-Fe^0 particles. With increasing Fa# values of the initial olivine, the produced np-Fe^0 particles demonstrated a tendency from spherical to angular, and abundant angular np-Fe^0 particles were observed in the experiments with Fa# ≥ 50.

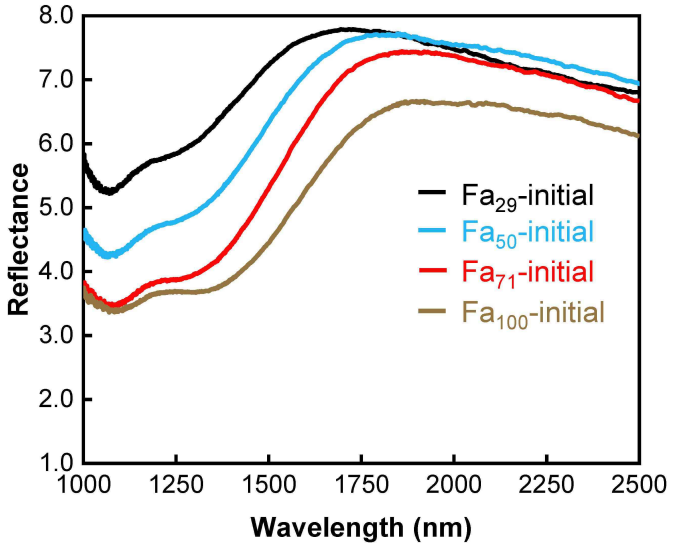

Fig. A.10. NIR reflectance spectra of the initial olivine samples Fa_{29}, Fa_{50}, Fa_{71}, and Fa_{100} without laser irradiation. Black line: Fa_{29}; blue: Fa_{50}; red: Fa_{71}; brown: Fa_{100}. With increasing Fa# values, the reflectance spectra of the initial olivine decreased in albedo, and the 1 μm absorption feature shifted to longer wavelengths.